5-14-2010

Structural Characterization and Thermoelectric Performance of ZrNiSn Half-Heusler Compound Synthesized by Mechanical Alloying

Jeffrey Germond
University of New Orleans

Structural Characterization and Thermoelectric Performance of ZrNiSn Half-Heusler Compound Synthesized by Mechanical Alloying

A Thesis

Submitted to the Graduate Faculty of the
University of New Orleans
In partial fulfillment of the
requirements for the degree of

Master of Science
in
Engineering
Mechanical Engineering

By

Jeffrey D Germond

B.S. University of Michigan, 2004

May 2010

TABLE OF CONTENTS

ABSTRACT

Thermoelectric (TE) ZrNiSn samples with a half-Heusler atomic structure were synthesized by mechanical alloying (MA) and consolidation by either Spark Plasma Sintering (SPS) or hot pressing (HP). X-Ray diffraction patterns of as milled powders and consolidated samples were compared and analyzed for phase purity. Thermal conductivity, electrical conductivity and Seebeck coefficient are measured as a function of temperature in the range 300 K to 800 K and compared with measurements reported for high temperature solid state reaction synthesis of this compound. HP samples, compared to SPS samples, demonstrate increased grain growth due to longer heating times. Reduced grain size achieved by MA and SPS causes increased phonon scattering due to the increased number of grain boundaries, which lowers the thermal conductivity without doping the base system with addition phonon scattering centers. Mechanical characterization of the samples by microindentation and depth sensing indentation for hardness and elastic modulus will be discussed.

Keywords: Mechanical Alloying – Milling – Heusler – half Heusler alloy – Thermoelectric materials – Thermoelectric properties – Spark plasma sintering – Hot Pressing – Seebeck coefficient – Electrical conductivity – Thermal conductivity – Figure of merit – Grain refinement – Mechanical properties – Indentation – Nanoindentation – Depth sensing indentation – Microindentation – Vickers – X-ray diffraction – Phonon scattering

1. INTRODUCTION

In 2008, the United States used 99.2 Quads (10^{15} BTU) of energy [1]. About 57.5 % of this energy was rejected or unusable and was lost as heat, sound, or light, etc. There is a great opportunity for energy recovery as the U.S. strives to become more energy efficient. One possible mode for this is through waste heat recovery, especially in the transportation industry, which is one of the least efficient in terms of energy usage. This inefficiency in energy use is one reason thermoelectric materials have gained more interest in recent years. Thermoelectric materials have the promising ability to convert heat directly into electricity without any moving parts. They have a multitude of compositions and fabrication methods that, when altered, can yield improvements in performance.

A high performance thermoelectric material has the characteristics of producing a large thermopower, conducting electricity well, and resisting heat conduction. Mechanical alloying is used as an alternate synthesis method to produce such a material with improved characteristic properties. Mechanical alloying is a solid state processing technique involving repeated welding, fracturing and rewelding of powder particles in a high energy ball mill. It allows for the preparation of nanocrystalline structures and intermetallic phases. In this research, elemental powders of Zr, Ni and Sn were ball milled to form a stable half-Heusler alloy. The main motive of this study is to show mechanical alloying is a viable, inexpensive, and quick method for producing high quality ZrNiSn half-Heusler TE compounds that show an improvement in thermoelectric performance.

There are two main parts of this study. The first deals with the synthesis of the mechanically alloyed powders as they are evaluated for phase formation, lattice structure parameters, thermal stability and particle size. The second explores the thermoelectric properties of the consolidated powders by evaluating electrical conductivity, thermal conductivity, the Seebeck coefficient and the figure of merit. The performance of the mechanically alloyed powders is compared with previously reported values in literature of the same compound synthesized by a high temperature method. Additionally, the mechanical properties of the mechanically alloyed thermoelectric samples are evaluated.

Chapter two is a summary of the past and current literature involving mechanical alloying, thermoelectric phenomena, and mechanical testing. Chapter three outlines the experimental details of ball milling, X-ray diffraction, thermoelectric measurements, and mechanical testing. Results of the synthesis and thermoelectric properties are presented in chapter four. The results obtained in this work are compared with previous studies. Conclusions are presented in the chapter five.

2. LITERATURE REVIEW

2.1 Mechanical Alloying

Mechanical alloying (MA) is a materials-processing method that can produce homogeneous materials starting from elemental powder mixtures. Constituent powders are alloyed by continuous grinding and crushing with the resultant compound often a proportional mixture of the starting materials. MA has a capability to produce non-equilibrium phases as well as novel crystalline and quasicrystalline phases. In addition, MA allows alloying of elements that are difficult to alloy by other methods [2].

The MA process was developed by John Benjamin in the 1960's at the International Nickel Company's Paul D. Merica Research Laboratory. The original goal of the project was to produce a nickel base superalloy for gas turbine applications. After multiple failed attempts, Benjamin proposed to use a high energy mill to favor plastic deformation and cold welding, and produce a refined internal structure. The eventual result of this endeavor was an oxide dispersion strengthened superalloy, attributed to MA [3]. Benjamin's work led to production of yttrium oxide and gamma prime hardening in a complex nickel-base superalloy, a small high speed shaker mill and eventually a larger ball mill to produce oxide dispersion strengthened alloys (ODS) on an industrial scale. MA became available to produce other ODS alloys, for coating applications and fast corrosion applications [4].

Following Benjamin's work, the field of MA expanded and combined with other mechanical and chemical processes to create many of the following sub-categories of milling. Reaction milling is a MA process that is accompanied by a solid state reaction. Cryomilling involves milling at cryogenic temperatures (<150 °C), which is often done in the presence of liquid nitrogen. Rod milling involves using long rod rotating in a cylindrical vial which exert shear forces on the material and reduce contamination. Mechanically activated annealing includes an isothermal annealing step in addition to the MA step. Finally, double mechanical alloying involves MA, heat treatment to form intermetallic phases, and additional MA for further refinement or reduced grain size [2].

2.1.1 Mechanism of Alloying

The basis of MA is the cycle of powder particles that are repeatedly flattened, cold welded, fractured and rewelded. When grinding balls collide, some amount of powder is trapped between them. This trapped powder undergoes two processes. The first is plastic deformation, which causes work hardening, failure and a reduction in particle size. The second is cold welding that takes place due to the new surfaces created by the fractured particles, causing an increase in size. These two processes will eventually balance and the powder will come to an equilibrium particle size. As this process continues, particles become more homogenous, until eventually the final powder is a single phase as seen in Figure 2.1 Steady state is reached when composition of every powder particle is the same as the proportion of the elements in the starting powder mix. Grain size decreases exponentially with time and can reach grain sizes on the nanometer scale. Because of this refinement ability, MA is extensively used for nanocrystallne material production [5,6]. An additional effect that accompanies grain refinement is an induction of mechanical strain within the sample [7]. As particles are repeatedly flattened, lattice strain accumulates and plateaus.

There are 3 different combinations of metals and alloys that are often used in MA: (i) ductile-ductile, (ii) ductile-brittle and (iii) brittle-brittle. Benjamin and Volin were the first to describe the mechanism of alloying on a ductile-ductile system [8]. The ductile components become flattened to platelet/pancake shapes and some quantity of powder becomes attached to the surface of the balls. This coating helps protect the system from contamination and prevents some wear on the surfaces of the balls. The flattened particles become work-hardened (increasing hardness) and fracture as brittleness increases. Benjamin also described a ductile-brittle system during the initial states of milling [4]. The ductile powder particles become flattened, but the brittle particles become fragmented and embedded in the ductile particles. As the ductile particles become work-hardened they also fracture. Lee and Koch demonstrated this reaction by MA of Ni (ductile) and $NiZr_2$ (brittle), where after 15 min of MA, the flattened Ni strips were embedded in a granular $NiZr_2$ matrix [9]. Lee and Koch also report MA of brittle-brittle systems between intermetallic compounds of $Ni_{11}Zr_9$ and $NiZr_2$. In this case the less ductile component becomes embedded in the more ductile component. After further milling the result was an amorphous $Ni_{40}Zr_{60}$ powder.

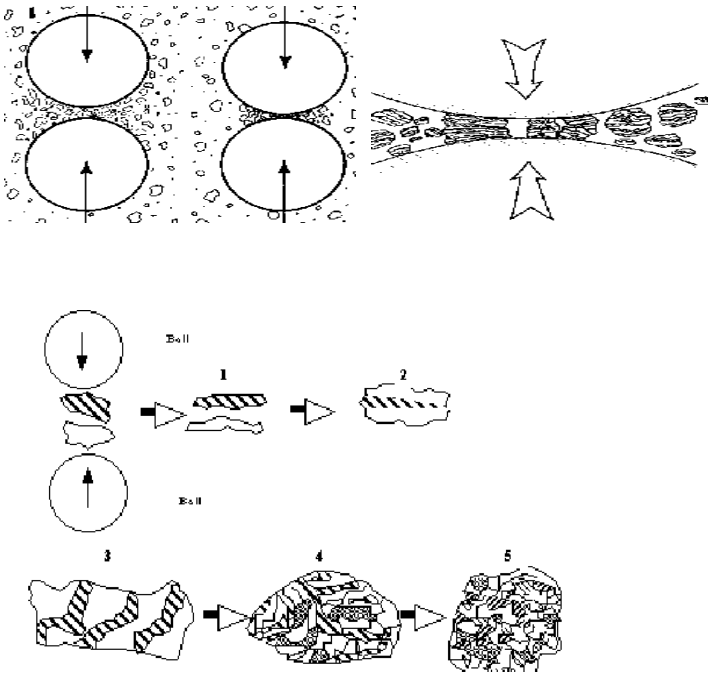

Figure 2.1: Mechanism of Alloying, cold welding and fracture (from [2])

2.1.2 Raw Materials

Starting materials consist of powders, often available commercially at a high purity, with particle sizes in the range of 1 – 200 μm. Powder size is not critical, as particle size is often reduced by the milling process. It is important that the powder particle size is smaller than the grinding ball. Powders can consist of pure metals, master alloys, prealloyed powders and refractory compounds.

2.1.3 Types of Mills

Milling equipment comes in different varieties. Different types can vary in their capacity, efficiency and additional arrangements for temperature control. Common types include shaker mills, planetary ball mills, attritor mills and commercial mills.

2.1.3.1 SPEX Shaker Mills

SPEX shaker mills accept small amounts (about 10 – 20 g) of powder at a time. Due to their size and high energy, they are often used in laboratory settings. These mills commonly hold one vial, but new dual models can accept two vials at a time. The vials are mounted in the clamp and swung energetically back and forth. The back and forth motion is accompanied by a lateral movement such that the vial traces the path of a figure 8. During an impact the balls strike the end of the vial, trapping some sample between the ball and the vial. The amplitude of the vial path is about 5 cm and completes about 1200 rpm. These parameters produce a ball speed of about 5 m/s, which is why the shaker mill is considered a high energy ball mill. See section 3.2 for more details on this system.

2.1.3.2 Planetary Ball Mills

Planetary ball mills can accept a few hundred grams of powder at a time. The vials are arranged on a rotating support disk. They rotate around their own axes and around the axis of the support disk. The vials and the supporting disk rotate in opposite directions which pins the grinding balls to the side of the vial. The balls rotate inwards, toward the center of the support disk, but eventually are overcome by the centrifugal force of the rotating support disk and travel across the diameter of the vial and impact on the opposite side of the vial. Planetary ball mills are able to produce higher velocities than a SPEX shaker mill, but frequency of impacts is much lower. Planetary ball mills are lower energy than a shaker mill. An example of a planetary ball mill is shown below in Figure 2.2.

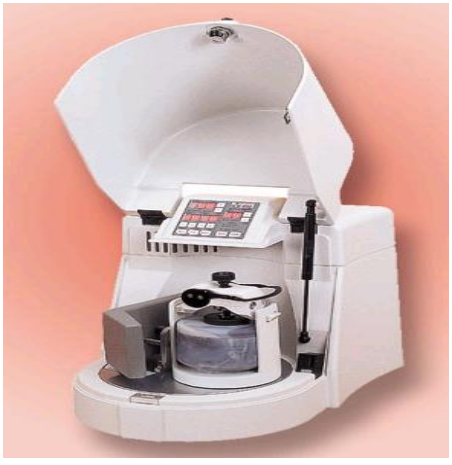

Figure 2.2: Planetary Ball Mill – Pulversitte 6

2.1.3.3 Attritor Mills

Attritors can accept quantities of powder ranging from 0.5 kg to 40 kg at a time. An attritor mill consists of a vertical drum with a series of impellers inside of it. The impellers are set at right angles to each other, shown in Figure 2.3. A motor causes rotation of the impellers which strike the grinding balls, which in turn, produce collisions between other balls, other impellers, the shaft and the container walls. The velocity of the grinding medium is on the order of 0.5 m/s, much lower than the shaker mill, and thus is considered a lower energy mill.

Figure 2.3: Attritor Mill Shaft and Impellers

2.1.3.4 Vibratory Mills

Vibratory mills are similar but less energetic than SPEX shaker mills. They impart energy to milling balls and powder by oscillating the milling vials at a specified frequency. While SPEX shaker mills agitate the milling balls and powder in 3 mutually perpendicular directions, the vibratory mill only agitates in one direction.

2.1.3.5 Commercial Mills

Commercial mills can process up to 3000 lb of powder sample at a time. They often consist of a rotating horizontal drum that is half filled with steel balls. As the drum rotates, the balls become pinned to the sides of the drum, until they reach the top where they loose contact with the edge and drop on top of the sample powder. Commercial mills are the lowest energy mills available, but produce the most sample at one time.

2.1.3.6 Uni-Ball-Mill

Uni-Ball-Mills are an improvement over the first milling technology. The concept was developed by Calka and Radlinski in 1991 and 1992. They imposed an external magnetic field over a horizontally rotating drum to control the motion of the milling balls. By imposing a higher strength field, they could create a higher energy milling environment. As shown in Figure 2.4, the path of the milling balls is altered by moving the magnets to different locations along the circumference of the drum and changing the field strength. The Uni-Ball-Mill became useful for being able to tune the amount of energy transferred by the mill to the powder [10].

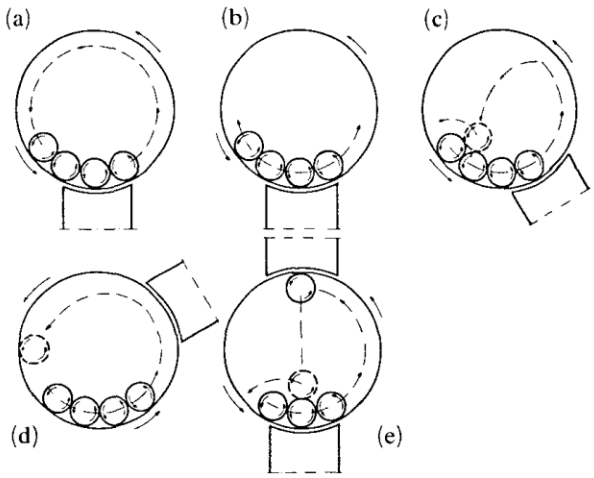

Figure 2.4: Modes of operation of the Uni-Ball mill. (a) High energy, high rotation frequency; (b) low energy, low rotation frequency; (c) high energy mode, two points of equilibrium; (d, e) high energy mode, intermediate rotation frequency, variation of mode (a) [10]

2.1.4 Process Variables

There are many variables that contribute to mechanical alloying. Manipulating some or all of the following variables will help lead to the desired phase or microstructure.

2.1.4.1 Type of Mill

As discusses in the previous section, there are many types of mills that differ in sample size, ball speed, frequency of collisions and energy level. Minutes in a higher energy mill can produce the same result as hours in a lower energy mill. Yamada and Koch demonstrated this in comparing TiNi samples milled with a SPEX shaker mill and a vibratory mill [11]. The SPEX mill produced rapid grain size reduction when compared to the vibratory mill. Shaker mills can be used to screen for alloy production and then a lower energy/larger capacity mill, such as an attritor or commercial mill, can be used to produce larger quantities of a sample.

2.1.4.2 Milling Container

Milling containers come in different shapes and are made of different materials. The choice of container is important as it is a source of contamination. Softer containers can allow for material to become dislodged from the inner walls of the container and incorporated into the powder. Common milling container types are hardened steel, stainless steel, hardened chromium steel, tempered steel, WC-Co, WC-Co lined steel, and bearing steel. Shape of the vial also can affect milling efficiency. Harringa et al. using $Si_{80}Ge_{20}$, showed that a SPEX shaker mill with a flat ended vial allowed alloying at a higher rate, in about 9 hours; while in a rounded end vial it took about 15 hours [12].

2.1.4.3 Milling Speed

Milling speed is directly related to the energy input to the powder, but has some limitations. For rotating mills, there is a maximum speed, above which, balls become pinned to the sides of the milling container, and impacts are significantly reduced. Also higher speeds can produce higher temperatures, which can be undesirable (or be desirable, depending on the application). Calka el al. demonstrated this effect by milling vanadium and carbon (VC) at different energy levels, which produced different final products [13]. Calka showed at medium energy, samples would form a nanostructure, but required a heating cycle to become an ordered VC compound. High energy resulted directly in a VC compound by milling.

2.1.4.4 Milling Time

The milling time required to achieve a desired phase depends on how efficiently the mill can transfer energy to the sample. This is directly influenced by the type of mill used, the intensity of the milling, the ball-to-powder ratio, and the temperature of milling. Milling for too short of a time will not allow the reaction to finish, but milling for an excessive amount of time may result in an increased level of contamination or a completely different product.

2.1.4.5 Grinding Medium and Ball-to-Powder Weight Ratio

Grinding balls are often made of steels and WC-Co due to their density and durability. Using a grinding container of the same material will also avoid cross contamination. During milling, powder can become coated to the balls and sides of the vial, which decreases the final yield. Using a combination of large and small balls can avoid excessive build up, as noted by Takacs and Pardavi-Horvath who were able to reduce the build up of Zn on the walls of the vial by using smaller balls [14].

Ball-to-powder ratio influences the amount of time it takes to complete the milling process. Higher energy mills can handle a lower ball-to-powder weight ratio due to the number of impacts that take place. An increase of ball-to-powder weight ratio causes the reaction to take place more quickly than a lower ratio [15]. An increased weight proportion of the balls increases the number of collisions per unit time per volume of powder, which increases the rate of energy transfer from the milling device to the sample and consequently the rate of alloying.

2.1.4.6 Process Control Agents

Process control agents (PCA), which are often organic compounds such as ethanol or hexane, can be added to the milling container to help control the rate of cold welding. This is desired in a system that has the propensity to cold weld but not fracture. This effect can cause a build up of welded particles and an imbalance to the system. Lee and Kwun used PCAs to control the build up of welding by the ductile components in their Ti-Al system [16]. They reported that as the amount of PCA increased, the mechanism of MA changed from substitutional diffusion to a penetration of metallic atoms into interstitial sites, the latter playing an important role in formation of an f.c.c. phase.

2.1.4.7 Milling Temperature

The temperature of milling can affect the rate at which a reaction takes place. The temperature can be lowered by dripping liquid nitrogen on the milling container or raised by heating the container. Milling at lower temperatures has the effect of further refinement of grains, and in some cases, increased likelihood of amorphous phase production [17,18]

2.1.4.8 Milling Atmosphere

Milling atmosphere can influence the purity of the powders during a reaction. Depending on the materials, care must be taken to ensure that the starting powders do not react with the atmosphere. Nitrogen has been found to react with metal powders and for this reason is not often used in MA [2]. Inert gases such as high purity argon are often used to ensure no unexpected reaction takes place. Vials can be filled and sealed in a closed atmosphere glove box, and then milled in a standard air atmosphere.

2.1.5 Uses of MA

Some common uses of MA are to produce solid solubility extensions, synthesize intermetallics, disorder intermetallics, and produce nanostructured materials.

2.1.5.1 Solid Solubility Extension

Mechanical alloying has the ability to synthesize equilibrium solid solutions in addition metastable, or non-equilibrium, supersaturated solid solutions. During mechanical alloying, the component elemental powders undergo significant interdiffusion, permitting the formation of a solid solution. With increasing milling time, the solubility increases, up to a supersaturation level that can be beyond the equilibrium value obtained with other solubility extension methods such as vapor deposition [19].

The mechanism for solubility is related to the idea of particle refinement. By decreasing the grain size through MA, the diffusion distance between particles is reduced. In addition, increased number of defects and increased temperature from the energy of milling can produce increased solubility. While MA can extend solid solubility, heating can, at times, cause the solid solution to revert to a lower solubility percent [20]. By this it can be reasoned that when a normally immiscible solid solution is formed by MA at room temperature, heat treatment may be able to separate the solvent and the solute and return the compound to an equilibrium phase. It is also reported that the use of a PCA can alter the solubility limit. For some systems solubility can increase in the presence of a PCA but in others, a PCA causes a decrease in solubility [21].

2.1.5.2 Synthesis of Intermetallics

MA has the capability to produce quasicrystalline and crystalline intermetallic phases. Crystalline phases can come in both equilibrium and metastable varieties. Quasicrystalline phases are phases that have non-crystallographic rotational symmetries and quasi-periodic translational order [22]. They were first obtained by MA in 1989 [23,24]. Eckart demonstrated with the use of a planetary ball mill that a quasicrystalline phase was the intermediate phase

between a stable equilibrium phase and an amorphous phase [24]. Metastable phases are not a common final product of MA. They are often found during intermediate stages of milling, but usually additional milling will continue the reaction to an equilibrium or amorphous phase. Martelli et al. obtained a metastable Ni-Sn phase after one hour of milling in a SPEX mixer/mill, which is of interest for this research, as it includes 2 of the 3 elements for formation of a half-Heusler system [25].

Equilibrium phases are of particular interest for thermoelectric applications. Thermoelectric materials can undergo numerous heating cycles and change of a phase during a heating cycle is not desirable. Equilibrium processing is sometimes accomplished with proper stoichiometric ratios of elemental powders and milling for sufficient time [26]. For some systems, however, additional steps need to be taken to achieve an equilibrium phase. Additional heat treatments are one option, as heating will relax internal strain accumulated by milling and allow a phase to become ordered. Robinson demonstrated this with the Heusler alloy Cu_2MnAl, which was milled for times up to 48 hours. After initial milling, the compound formed a metastable phase. Upon heat treatments, a stable Heusler phase formed exhibiting properties similar to the same compound formed by alternate synthesis methods [27]. Atzmon also demonstrated an unusual synthesis of an intermetallic phase. Production of a NiAl phase involves combustion synthesis, which only takes place after milling is interrupted. A thermocouple attached to the side of the milling vial showed an exothermic reaction took place within 60 seconds of milling, after the vial sat at room temperature for 30 minutes following its initial bout of milling [28].

2.1.5.3 Disordering of Intermetallics

Common methods of disordering alloys include irradiation [19], rapid solidification [29] or heavy plastic deformation. As discussed earlier, one of the direct results of MA is heavy plastic deformation. Repeated flattening and deformation of a sample results in dislocations, vacancies, stacking faults and altered grain boundaries, which all lead to the formation of a disordered phase. Anti-site disorder results when atomic species occupy the improper sublattice, or switch places. This produces strain within the lattice. Triple-defects occur as a result of anti-site disorder, but only one atomic species occupies the improper sublattice. The result is additional vacancies on the first sublattice that the first atomic species vacated and additional occupancy on the second sublattice. Redistribution of interstitials occurs when the actual lattice changes, such as from an octahedral to a tetrahedral coordination [30].

2.1.5.4 Nanostructured Materials

Nanostructured materials have grain sizes in the range of 1 – 100 nm, and are often desirable as material properties in the nanometer scale are often different from material properties on the macro scale [31]. Nanocrystalline materials demonstrate increased strength, high hardness, and high diffusion rates, which reduce sintering times for sample consolidation. MA is able to produce bulk quantities of nanostructured materials using simple equipment [6]. Nanostructured materials can be made in both single phase and multiphase varieties. Hellstern et al. milled a Ru sample for 32 hours an observed a significant reduction in grain size from 125 microns to less than 20 nm. No new phase was formed but they did observe an increase in specific heat from only grain size refinement [32]. Eckert et al. used Al, Cu, Ni and Pd samples

and examined their particles sizes at various stages during milling. They determined that the final grain size achieved is a result of the competition between the heavy mechanical deformation introduced during milling and the recovery behavior of the metal. They also noted a correlation, showing that a material with higher melting point and bulk modulus demonstrate a smaller final grain size [33].

2.1.5.5 Amorphization

An alloy that lacks a crystal structure is classified as an amorphous alloy. MA can often drive a solid state amorphization reaction (one that does not pass through a liquid or gaseous state). Amorphous phases have been synthesized by MA from starting materials of blended elemental powders, prealloyed powders and/or intermetallics, mixtures of intermetallics or mixtures of intermetallics and elemental powders. Suryanarayana provides an extensive list of amorphous phase systems. He noted the critical milling parameters that influence the formation of the amorphous phase [2]. Amorphization by MA can be more powerful than other methods. For example, Lee and Koch report on the formation of amorphous Ni_xZr_{1-x} in the range $0.24 \leq x \leq 0.85$ by mechanical alloying [9]. This range is larger than the range produced by melt-spinning techniques of $0.10 \leq x \leq 0.22$ and implies less dependence on the composition of the sample for amorphous phase production by MA. Lee et al. demonstrated similar behavior with a Ni-Ta system, showing that there was a larger amorphization range (based on composition), than other preparation methods such as rapid quenching or electron-gun deposition [5].

2.2 Thermoelectrics

The thermoelectric effect is the direct conversion of a temperature gradient into an electric potential. A temperature gradient imposed on a thermoelectric material mobilizes charge carriers, electrons or holes, and causes them to diffuse from the higher temperature area to the lower temperature area. Thermoelectric power can be generated by placing this voltage potential into a closed circuit.

Thermoelectric phenomena were first observed in 1823 by T. J. Seebeck. Seebeck reported results of experiments in which a compass needle was deflected when placed in the vicinity of a closed loop formed by to dissimilar conductors, one of which was heated [34]. Seebeck originally believed this was an observation of a magnetic effect. Later review showed it was an observation of the thermoelectric effect caused by electric current flowing through the circuit. The Seebeck coefficient *S,* expressed in volts per degree, was attributed to this research.

A complimentary effect was discovered by J. C. Peltier. Peltier observed temperature changes near the junction of dissimilar conductors when a current passed [35]. Peltier's observations were explained by Lenz in 1838 [36]. Lenz showed that by changing the direction of current flow through a bismuth-junction he could both produce a cooling effect to freeze water and produce a heating effect to melt ice. A third thermoelectric effect was predicted and shown experimentally by W. Thomson in 1851 [37]. He established a relationship between the Seebeck and Peltier coefficients and predicted the Thomson effect. The Thomson effect relates to the heating or cooling in a single homogeneous conductor when a current passes along in the presence of a temperature gradient.

Altenkrich provided a theory of thermoelectric generation and refrigeration that defined "good" thermoelectric materials as those that generate a larger amount of thermopower, retain heat at the junctions, and minimize joule heating [38-39]. These effects correspond to material properties of a large Seebeck coefficient, low thermal conductivity and low electrical resistance, respectively. These desired properties are arranged in an expression for a so-called figure of merit Z:

$$Z = \frac{S^2\sigma}{\kappa} \tag{2.1}$$

where S is the Seebeck coefficient, σ is the electrical conductivity and κ is the thermal conductivity. The numerator, $S^2\sigma$, is often referred to as the power factor. S is the dominant term in Equation 2.1 as it is squared, so a large Seebeck coefficient is crucial to a large Z. The unit of Z is 1/K, which leads to a nondimensional figure of merit by multiplying Z by the absolute temperature of the device, T. ZT has become known as a measure of the efficiency of a TE material.

Thermoelectric materials are categorized as n-type or p-type depending on whether the respective charge carriers are electrons or holes. The fundamental difference between p-type and n-type is the direction the current flows. By sandwiching both n and p-types between two electrically insulating and thermally conducting ceramic plates, a thermoelectric module can be formed as shown in Figure 2.5. A temperature difference across the module will allow a steady current to be delivered to some external load, and the module acts as a thermoelectric generator. Similarly by inducing a current through the module, it will induce a temperature difference, and the module will act as a refrigerator or a heater.

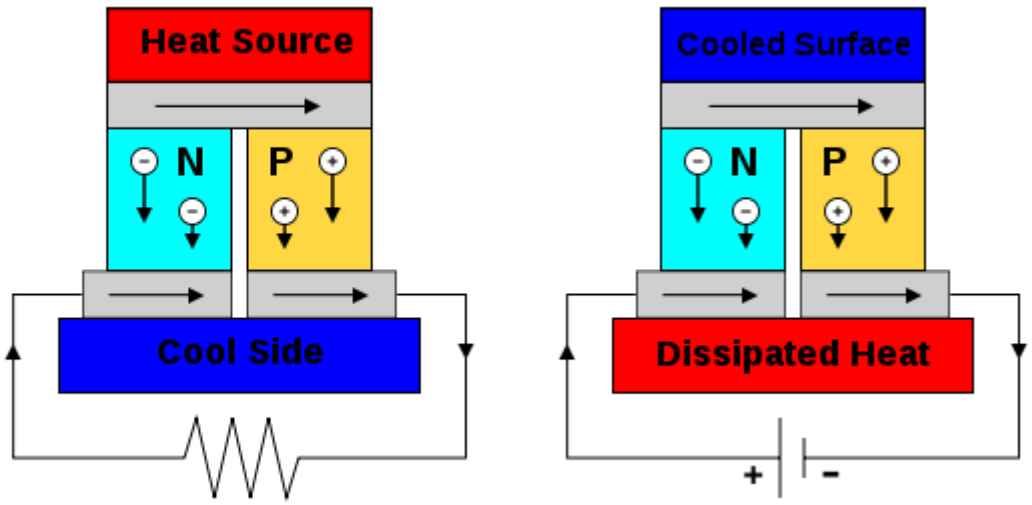

Figure 2.5: Thermoelectric Generator (left) and Refrigerator (right) [107]

2.2.1 Transport Properties.

Electrical conductivity is a measure of a material's ability to conduct an electric current; it is the inverse of electrical resistivity. Related to thermoelectric materials, a large electrical conductivity is desired to maximize the amount of current flowing through the device. Low electrical conductivity implies high electrical resistivity and excessive joule heating. Due to the temperature dependence of the dimensionless figure of merit, joule heating is not desired.

Thermal conductivity is a measure of a material's ability to conduct heat. There are two methods of heat conduction that take place in a thermoelectric material. The first is electronic thermal conductivity and relates to heat carried by the electrons in a material; it is directly proportional to the electrical conductivity by the Wiedemann-Franz Law:

$$\kappa_{electronic} = \sigma L T \tag{2.2}$$

where L is the Lorenz number. The second is lattice heat conductivity, which can be described in terms of carriers called phonons. A phonon is a quantum of energy relating to a mode of vibration in a crystal lattice. The total thermal conductivity, κ_{total}, is described by the equation:

$$\kappa_{total} = \kappa_{electronic} + \kappa_{lattice} \tag{2.3}$$

High thermal conductivity will reduce the performance of a thermoelectric device. Because electrical conductivity and thermal conductivity are partially coupled by Equations (2) and (3), increasing electrical conductivity will lead to and increase in thermal conductivity if $\kappa_{lattice}$ remains constant. New research, however, has shown promise for decoupling electron transport from phonon transport using nanoscale gaps, creating non-equilibrium between electrons and phonons [40].

The absolute Seebeck effect (ASE) is defied as an electric potential generated within any isolated conducting material that is subjected to a temperature gradient [37]. It is related to the absolute Seebeck coefficient (ASC), the relative Seebeck emf (RSE) and the relative Seebeck coefficient (RSC). The ASC is defined as the instantaneous rate of change of the absolute Seebeck effect with respect to temperature at a given temperature. The RSE is the voltage resulting from the difference between the internal potentials, and the RSC is the instantaneous rate of change of the RSE with temperature at a given temperature.

2.2.2 Figure of Merit

The figure of merit is usually written as Eq. 2.1, but its true definition involves both a p-type and an n-type material:

$$Z = \frac{\left(S_p - S_n\right)^2}{\left(\kappa_p \rho_p^{1/2} + \kappa_n \rho_n^{1/2}\right)^2} \tag{2.4}$$

Equation 2.4 is difficult to use when attempting to identify a good TE material, so the figure of merit of a single material is defined by Equation 2.1. Ultimately the figure of merit is limited by

the efficiency of the Carnot cycle (Equation 2.5), which gives the maximum efficiency of a heat engine operating at two different temperatures.

$$\eta = \frac{(T_1 - T_2)}{T_1} \tag{2.5}$$

The figure of merit modifies Equation 2.5 by adding a term based on Z

$$\eta = \frac{(T_1 - T_2)}{T_1} \cdot \frac{\left(\sqrt{1 + ZT_M} - 1\right)}{\left[\left(\sqrt{1 + ZT_M} + \frac{T_2}{T_1}\right)\right]} \tag{2.6}$$

where $T_M = (T_1 + T_2)/2$. The additional term in Eq. 2.6 prevents the efficiency of a TE device from reaching the ideal Carnot cycle efficiency [41]

2.2.3 Material Systems

There are numerous different material systems undergoing research that have promising thermoelectric potential. Potential TE material systems were recently reviewed by Kanatzdis [108], some of the figures of merit materials are shown in Figure 2.6.

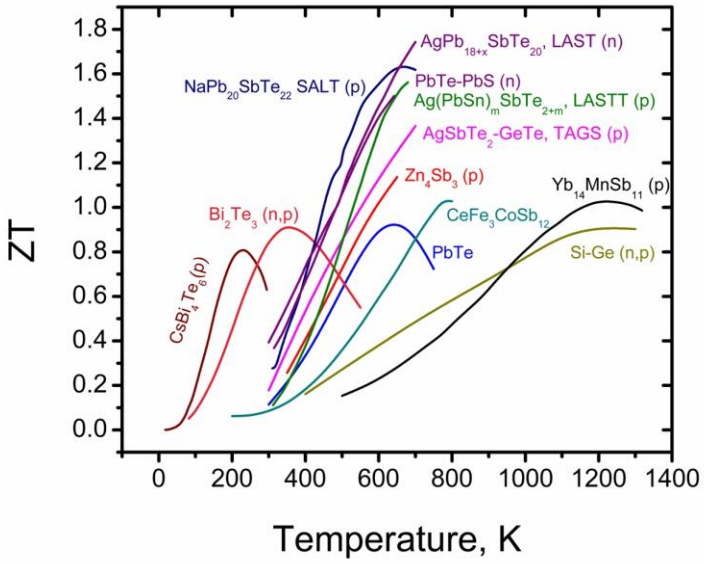

Figure 2.6: Thermoelectric Materials [108]

As a note, many of the compositions shown in the plot contain Te, which is known as one of the rarer elements found on earth. This scarcity rules out mass production of Te based thermoelectric materials. The most desirable TE materials will have a high figure of merit but a low cost of production. Cost of production will increase based on the rarity of the constituent

elements and the method of manufacturing. The systems studied in this research are described in the following section.

2.2.4 Heusler and Half-Heusler Alloys

Heusler alloys were first studied by Friedrich Heusler in 1903 with the composition $MnCu_2Al$ [42]. This structure demonstrated properties that varied with both heat treatment and composition and were later termed 'Heusler' alloys [43]. Knowlton and Crawford noted that specimens that were cooled quickly were exceptionally brittle and appeared strongly magnetic. But when cooled slowly had reduced magnetic quality but were much less brittle. The rate of cooling had an effect the crystal structure formation. Heusler phases are intermetallics with a particular composition and f.c.c. crystal structure. Some Heusler materials were noted to have thermoelectric properties [44]. Half-Heusler phases are similar in structure to Heusler phases. Jeitschko studied transition metal stannides with MgAgAs-type structure (space group $\bar{F}43m$), which were termed 'half-Heusler' alloys [45]. Half-Heusler alloys were later explored by Aliev and Cook, who measured the band gap of about 0.2 eV on a particular subset of these structures with MNiSn (M = Zr, Hf, Ti) [46,47]. Aliev reported unusual transport and optical properties while Cook recognized that these materials potentially useful thermoelectric materials. He examined TiNiSn and reported a power factor of 25 $\mu W/cm\text{-}°C^2$.

2.2.5 High Temperature Synthesis

A thermoelectric compound starts as a mixture of elemental powders which need to be annealed or alloyed in some way. Arc melting is quite common among some of the earliest groups working with half-Heusler systems [48-51]. It involves bringing the sample in direct contact with an electrical arc. This was completed 2 – 3 times per sample to ensure homogeneity. Uher showed that an additional, separate annealing process caused an increase or decrease in thermal conductivity, which depended on the number of elements in the system [49]. Longer times at high temperature allowed the structure to become increasingly well ordered, which caused an increase in thermal conductivity for 3 element systems and a decrease for 4 or more element systems. The additional element which substituted into the lattice structure, served as phonon scattering center, which decreased the lattice thermal conductivity. Hohl used a solid state reaction method to produce his samples [52]. Hohl also used a variety of added dopant elements to attempt to reduce the thermal conductivity of the samples. He realized that some dopants had vapor pressures so high that arc melting would cause loss of dopant. He dissolved dopants in tin before arc melting to preserve as much sample as possible. Loss of materials due to vaporization is one reason other methods of synthesis were investigated. A solid state reaction method, with a sample sealed within a quartz ampoule, has been used to eliminate the vaporization [53].

2.2.6 Mechanical Alloying as a Synthesis Method

Mechanical alloying has become an alternate method for synthesis of TE materials. It has the advantage of a short cycle time, when compared to the high-temperature synthesis methods. Mechanical alloying by its nature causes grain refinement which can affect transport properties of a TE material.

Alloying has been attempted on different compositions of TE materials. Similar to high temperature synthesis, MA synthesis is controlled by many variables. Milling energy must be high enough to allow for MA to take place. If a lower energy mill is used, it can take many hours, or even days to obtain the desired result. Cook et al. demonstrated that in some cases the alloy does not form unless the mill has sufficient energy [54]. He attempted the uses of a planetary ball mill but after 3 days of milling without formation of an alloy, used a SPEX mixer/mill which formed an alloy in less than 6 hours. Mikami et al. produced a Fe_2VAl Hesuler alloy with a grain size on the order of 100 nm, strictly by MA and sintering for consolidation [55]. Additional studies involving synthesis of TE materials by MA are as follows: TiCoSb [56], TiNiSn [57], Cu_2Te [58], SiGe [54], Ag_2Se [59], $CoSb_{3-x}Te_x$ [60], $La_{3-x}Te_4$ [61], Bi_2Te_3 [7], Sb_2Te_3 [62], and Bi_2S_3 [63]. In the preceding cases mechanical alloying was used to modify the transport properties in some way, most commonly to reduce the lattice thermal conductivity. The grain refinement capability of mechanical alloying produces more grain boundaries, which induces additional phonon scattering and a subsequent reduction in lattice thermal conductivity.

2.2.7 Half-Heusler Thermoelectric Compounds

TE materials, having a semiconductor nature, seem to have both high electrical conductivity and high thermal conductivity. While the high electrical conductivity is beneficial to the figure of merit, the high thermal conductivity is detrimental. Some of the most recent research focuses on reducing the thermal conductivity of TE materials, with half-Heusler alloys contributing a significant portion of the research.

In 1996 Cook was one of the first to measure transport properties on a half-Heusler system using TiNiSn [47]. Later work began on the ZrNiSn system. [48,50,52,64,65]. Uher et al. investigated the transport properties of the base ZrNiSn system, reporting favorable electrical resistivity and thermopower [64]. He also used substitution to modify the transport properties, creating such samples as $Zr_{0.5}Hf_{0.5}NiSn$ and $Zr_{0.5}Hf_{0.5}NiSn_xSb_{1-x}$, noting that the addition of Sb improved the electrical conductivity significantly. Antimony (Sb) has one additional electron compared to Tin (Sn), which gave the samples a more metal-like behavior and an increase in electrical conductivity. Cook verified previous results, exploring the $Zr_{1-y}Hf_yNiSn_{1-x}Sb_x$ system and, similar to Uher, noted that the electrical conductivity was similar to other state of the art materials, but thermal conductivity remained too high [48]. Additional work involved doping the ZrNiSn system with niobium, tantalum, indium and bismuth [52, 49]. Samples of this nature showed some reduction in thermal conductivity and up to a maximum ZT of 0.5 around 700 K. Shen et al. continued with improvements to the ZrNiSn system by introducing doping on the Ni site and using a high temperature solid state reaction instead of the traditional arc melting [53,66,67]. The highest figure of merit achieved was ZT = 0.7 with the compound $Zr_{0.5}Hf_{0.5}Ni_{0.5}Pd_{0.5}Sn_{0.99}Sb_{0.01}$. At that time, it was the highest figure of merit reported for the system and Shen concluded that a further reduction in thermal conductivity would produce an even higher figure of merit [67].

Work on the ZrNiSn system continued with attempts to reduce thermal conductivity. Huang et al. used doping of ZrO_2 nano-particles to introduce additional phonon scattering centers [68]. The result was a maximum 35% reduction in thermal conductivity and a slight increase in figure of merit. Yu et al. attempted an alternate high temperature synthesis method, using levitation melting and spark plasma sintering (SPS) [69]. Yu also compared SPS to hot pressing

(HP), with SPS samples yielding better performance. Increased figure of merit by SPS was attributed to low packing density achieved by HP.

A number of other studies compare other half-Heusler alloys. TiCoSb was synthesized by mechanical alloying, which produced a half-Heusler phase and a reduction in thermal conductivity [26,56]. Extensive research on the base compound TiNiSn has also been completed, showing similar reduction in thermal conductivity by doping of Zr at Ti, Sb at Sn sites with the addition of mechanical alloying [57,70-72]. The ZrCoSb system yielded similar reductions in thermal conductivity with substitutional disorder of Hr on the Zr site, Ir on the Co site and Sn on the Sb site [73].

Summarizing the above, by doping the system with Sb, electrical conductivity increases. By doping the system with additional mass scattering centers thermal conductivity decreases. These effects have minimal effect on the Seebeck coefficient and demonstrate an improved figure of merit with the most improvement coming from a reduction in thermal conductivity.

2.3 X-ray Powder Diffraction

X-rays were discovered in 1895 by W. C. Rontgen and lead to three major branches of science: X-ray radiography, X-ray crystallography and X-ray spectrometry. X-ray radiography uses that property that X-rays are relatively absorbed by matter as a function of the average atomic number and density of the matter in question. This is the field of X-ray science that is used quite often in the medical field to diagnose broken bones. X-ray crystallography was born in 1912 from experiments conducted by Max von Laue, where he confirmed the wave characteristics of X-rays. Powder diffffracometry is a subfield of X-ray crystallography. X-ray spectrometry is the third branch of science developed, and it also began in the early part of the 20^{th} century [74].

2.3.1 X-ray Origins and Production

X-rays are short-wavelength, high-energy beams of electromagnetic radiation. Similar to all electromagnetic radiation, X-rays have wave particle duality; meaning they exhibit both wave-like and particle-like properties. X-rays are characterized by the following equations:

$$\nu = \frac{c}{\lambda} \text{ and } E = h\nu \tag{2.7}$$

where λ is wavelength, ν is frequency, E is photon energy, c is the speed of light and h is Planck's constant. These equations can be combined to describe the energy or an X-ray photon:

$$E = \frac{hc}{\lambda} \tag{2.8}$$

Equation 2.8 allows for easy conversion between energy of the photon and X-ray wavelength. For example, Cu $K\alpha_1$ radiation has energy of about 8.05 keV, which corresponds to a wavelength of 1.541 Å.

X-rays are produced when fast moving electrons strike matter. A high speed electron can displace a tightly bound electron in the atom's inner shell near the nucleus, and cause the atom to

ionize. An electron from an outer shell may fall in the vacant space, which results in the emission of an X-ray [75]. For powder diffractometry purposes, this sequence occurs in a controlled manner, in an X-ray tube as shown in Figure 2.7.

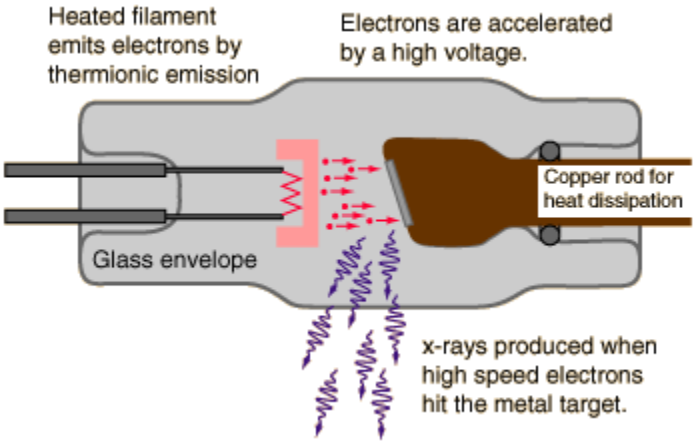

Figure 2.7: Schematic of an X-ray tube [112]

2.3.2 Diffraction of X-rays

For diffraction it is useful to think of X-rays as electromagnetic waves proceeding outward from a source. In 1912, Max Von Laue described X-ray diffraction as follows. Electrons in the path of such a wave are excited to periodic vibrations by the changing field and become sources of electromagnetic waves of the same frequency and wavelength. These electrons form a pattern of spherical wave fronts and effectively scatter the original beam. A periodic array can scatter radiation coherently forming constructive interference, or incoherently forming destructive interference [75]. In 1913 William Lawrence Bragg developed a simpler way for understanding X-ray diffraction from crystal planes [76]. He used a series of regularly spaced crystal planes to describe the crystal structure. From Figure 2.8, incident wave paths 1 and 2 are in phase, but when reflected, 1' and 2' are only in phase if the distances BC + CD are equal to an integer multiple of the wavelength. Using the geometry shown in the figure, where both incident and diffracted beams follow a trajectory θ degrees off the horizontal and with spacing between planes *d*, the distances $BC = d\sin\theta$ and $CD = d\sin\theta$.

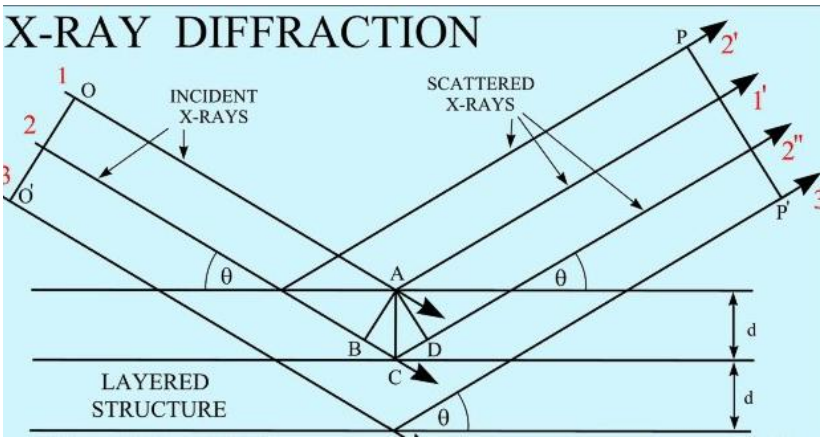

Figure 2.8: Geometry of Bragg "reflection"

The Bragg relationship can be derived for the necessary condition for constructive interference to occur:

$$BC + CD = n\lambda = 2d\sin\theta \tag{2.9}$$

where n is an integer and λ is the x-ray wavelength. Equation 2.9 is known as the Bragg Law and for a specific λ and d there are multiple values of θ where constructive interference occurs.

2.3.3 The Reciprocal Lattice

A useful method for describing and explaining diffraction phenomena was developed by Ewald in 1921 [77]. Ewald called his idea the reciprocal lattice. A reciprocal lattice is used because of its geometric convenience but it does not have any physical significance. The reciprocal lattice is constructed in reciprocal space and has a has a dimension $1/d$, where d is the spacing between crystal planes. The reciprocal lattice will not be detailed in this research. For in depth discussion on reciprocal lattice see [74] and [75].

2.3.4 Intensity of Diffraction

During X-ray diffraction (XRD), the incident beam remains focused on the sample while the incident angle changes. The intensity of the diffracted beam is measured at each angle, and for certain angles, constructive interference occurs, producing peaks. The locations of these peaks provide information about the lattice structure of the sample, including lattice spacing, shape, and elements that comprise the structure. Peak intensity is related to the number of reflected X-rays at a given Bragg angle, and is directly influenced by the crystal structure.

2.3.5 Broadening of Peaks

Scherrer showed that X-ray diffraction lines tend to broaden as the crystallite sizes become smaller [78]. He proposed a simple formula relating D, the mean dimension of the crystallites to the breadth of the XRD line:

$$D = \frac{K\lambda}{\beta \cos\theta} \tag{2.10}$$

Where β is the pure breadth of a powder reflection free of all broadening due to the experimental method, *K* is a constant approximately equal to unity, and λ is the X-ray wavelength. It is worth noting that *K* is dependent on the way β is measured. β can be measured as the angular width at half maximum intensity or the integral breadth (the angular width of a rectangle with the same integrated area of the peak in question). Patterson outlines some of the work done regarding the value of *K* in relation to β [79].

Following the work of Scherrer, in 1944 Stokes and Wilson reported on line broadening caused by cold working in metals [80]. They observed that as metal is broken up, the diffraction lines would broaden due to this distortion of crystals. They also proposed a formula to estimate the amount of broadening due to strain of a particle:

$$\eta = \beta \cot\theta \tag{2.11}$$

Where the pure spectral line breath is β and the apparent tensile strain is given as η.

The work of Sherrer and Stokes and Wilson was later combined in 1953 by Williamson and Hall [81]. Williamson and Hall noted that the broadening of the peak based on sizes was directly proportional to $\frac{1}{\cos\theta}$ while the broadening based on strain was directly proportional to $\tan\theta$. The combination of equations 2.10 and 2.11 lead to an equation that can separate the broadening effects of size and strain:

$$\beta \cos\theta = \frac{K\lambda}{D} + \eta \sin\theta \tag{2.12}$$

A plot of a diffraction patterns peaks using equation 2.12, with $\sin\theta$ on the x-axis and $\beta\cos\theta$ on the y-axis, should take the appearance of a straight line with slope of η and y-intercept of $\frac{K\lambda}{D}$.

Additional methods of separating size and strain are also used. Zakeri et al. discusses alternate methods [7,62]. The first, also discussed by Klug and Alexander [75], assumes that strain broadening and size broadening cause two different types of peak shapes. Strain broadens the peak with a Gaussian shape, while small grain size broadens the peak with a Lorentzian (or a Cauchy) shape. These effects can be separated with the following equation:

$$\frac{\beta^2}{\tan^2\theta_0} = \frac{K\lambda}{D}\left[\frac{\beta}{\tan\theta_0 \sin\theta_0}\right] + 16e^2 \tag{2.13}$$

Where β is the pure line profile width and half maximum, θ_0 is the position of the peak analyzed, and *e* is the maximum strain ($\eta = 4e$). Plotting the term $\left[\frac{\beta}{\tan\theta_0 \sin\theta_0}\right]$ on the x-axis and $\frac{\beta^2}{\tan^2\theta_0}$ on the y-axis should result in a straight line with slope $\frac{K\lambda}{D}$ and intercept $16e^2$.
Another method is based on the assumption that both size and strain profiles are assumed to be Gaussian:

$$\beta^2 \cos^2\theta_0 = \left(\frac{\lambda}{L}\right)^2 + 16e^2 \sin^2\theta_0 \tag{2.14}$$

Equation 2.14 is very similar to 2.12 above. In Equitation 2.14 every term is squared and *K* is assumed to be one. Even with a variety of methods for size and strain analysis, it is not always possible to separate the effects. Small peaks can be difficult to separate from background radiation which can cause scatter in the size/strain plots or even a negative intercept, which does not make sense in terms of crystallite size. Zakeri et al. evaluated each of these methods on Sb_2Te_3 (Equations 2.12, 2.13, 2.14) but was not able to separate size and strain [62]. He determined that anisotropy of the crystal structure was preventing accurate size/strain separation.

2.4 Mechanical Properties

TE materials have potential to be used in many different fields if their efficiency improves. Their current, most recognized, use is in space exploration where they harness heat from radioactive isotopes to power onboard devices. In addition, TEs are becoming more attractive to the automotive and aerospace industry for both waste heat recovery and for potential cooling applications. A prerequisite for commercial use, besides efficient power production or refrigeration capability, is mechanical robustness. TE materials mounted around the muffler on an automobile would need to have the ability to undergo dramatic, repetitive thermocycling, but also resist cracking or failure from vibration due to the road. For this reason, elastic modulus, hardness, bending strength, and fracture toughness become important properties.

2.4.1 Mechanical Properties of Thermoelectric Materials

Standard tests for elastic modulus are described by the American Society for Testing and Materials. The test specimen is loaded uniaxially and load and strain are measured, either incrementally or continuously. The axial stress is determined by dividing the load value by the specimen's original cross sectional area. The appropriate slope is then calculated from the stress-strain curve, which may be derived under conditions of either increasing or decreasing load [82]. The slope of the line is the elastic modulus, E, and is defined as:

$$E = \frac{\sigma}{\varepsilon} \tag{2.15}$$

where σ is the stress and ε is the strain. Test specimens are required to have a uniform cross section and be free of residual stresses. A stronger or stiffer material would demonstrate a larger value of elastic modulus. The modulus for aluminum is on the order of 70 GPa, for steel around 200 GPa and for diamond over 1100 GPa.

Bending strength tests involve taking a specimen and subjecting it to known bending configuration. An example of three point bending is shown in figure 2.9. Monitoring the response of the specimen under the bending forces allow for a bending, or flexural, modulus to be determined. The maximum bending strength of a specimen can also be determined. Bending tests are easier to conduct as the sample only needs to have a regular geometry and does not need to be cut or drilled for mounting, which is sometimes required for uniaxial load tests.

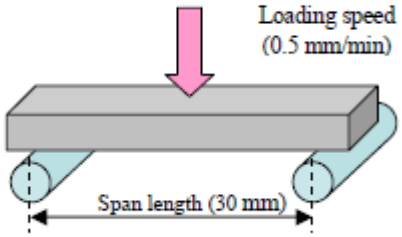

Figure 2.9: Three point bending test (from [84])

Lead telluride TE samples characterized by 3 point bending demonstrated that n-type materials displayed higher strength and ductility when compared to p-type materials [83]. Similarly, Urata et al. discussed the bending strength of $Ca_3Co_4O_9$ p-type and $CaMnO_3$ and $LaNiO_3$ n-type materials, showing a correlation between the relative density and the bending strength [84]. In Urata's study, there was no difference in bending strength between the p-type and n-type materials. Other systems studied by this technique include $(Bi_{1-x}Sb_x)_2(Te_{1-y}Se_y)_3$, showing difference in bending strength dependent on direction of extrusion, and $(Sb_2Te_3)_{75}(Bi_2Te_3)_{25}$, noting that higher bending strength is correlated with smaller grain size [85,86].

2.4.2 Indentation Techniques

Thermoelectric samples can be difficult to measure with tension tests. They are problematic to cut into proper geometry, and they are small. They are often pressed cylindrical pellets about 10 mm in diameter and 1.5 – 4 mm thick. In addition, there is often only a limited amount of a sample, so and subjecting it to one destructive test is not ideal. Another method used for determining material properties is indentation. Indentation methods allow for a small sample to be indented by diamond tip and elastic modulus and hardness extracted from either the feedback from the sample while the indent is occurring or the resulting impression. Microindentation follows the procedure of indenting the sample with a known load and measuring size and appearance of the resulting indent. Nanoindentation or depth sensing indentation refers to a precisely controlled and monitored diamond tip that indents samples. This device measures the feedback of the sample under loading and extracts modulus and hardness values from the data. Both indentation methods provide data that can determine a variety of mechanical properties, such as modulus, hardness, and fracture toughness, which are useful in sample characterization.

2.4.3 Microindentation

The procedure for measuring hardness is straight forward. A residual deformation is optically measured, and using the force from initial load, a hardness value is determined. Hardness is a property that is specific to the indenter. The shape, or type of diamond used will directly influence the measurement. Common shapes are Vickers, Knoop, cube corner, and spherical indenters. Vickers and Knoop Geometries are shown in figure 2.10. On a Vickers tip, opposing indenter faces are set at a 136 ° angle to each other. For Knoop, long side faces are set at a 172 °, 30 minute angle to each other. Short side faces are set at a 130 ° to each other.

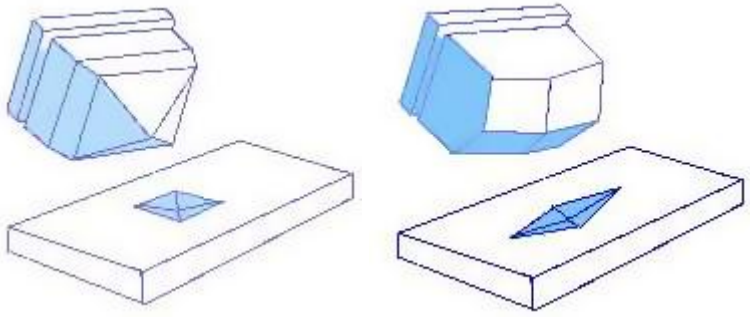

Figure 2.10: Vickers and Knoop indenter geometries (from [109])

Vickers hardness has been used to characterize TE materials [83,87]. Because a Vickers indent only provides one property of a material, it is often used in conjunction with another measurement, such as 3 point bending, to produce a more complete characterization. A technique has been developed to extract an elastic modulus measurement from the residual indents left by a Vickers and Knoop indents [88]. Marshall used the idea that Knoop indent will recover more along the short diagonal, than on the long diagonal and developed a useful formula for materials with sufficiently high ratio of Hardness/Modulus. This technique has been employed on some systems of TE materials and has given good agreement with other measurements [89].

2.4.4 Nanoindentation

Nanoindentation can directly measure both the elastic modulus and the hardness of a material from a single indent. Theory on nanoindentation is summarized by Oliver and Pharr [90]. It is also briefly described in section 3.5.

Providing an elastic modulus in addition to hardness from the information in one indent has proven useful for TEs. A notable study examined lead-antimony-silver-tellurium (LAST) TEs and developed a formula to predict the hardness of the material based on its composition [91]. Ren used a combination of microindentation and nanoindentation to ensure accuracy in his results.

2.4.5 Other Tests

2.4.5.1 Fracture Toughness

Fracture toughness is the property of the material that describes its ability to resist crack growth. Most often it is measured by pre-cracking a material and placing it in a controlled loading scheme that will propagate the crack. Analyzing the crack response with respect to the increasing load gives information about the ability of the material to resist crack growth. An alternate method for fracture toughness measurement is by indentation methods [92-94]. Indenting with an indenter of known shape with sufficient load can produce half-penny shaped cracks. Analyzing the crack size, related to the indent size, yields information about the fracture toughness of the material [95]. Further work has been completed, classifying 3 methods: direct, indirect, and modified for characterization of a material by indentation fracture [96]. Examples of traditional methods and direct indentation methods are found for thermoelectric materials and are described as follows. Ueno et al. used a single edged notched beam configuration for evaluating crack growth in Zn_4Sb_3 [97]. Zhao et al. used a Vickers indent at high load to show that as nano particles were added to his system, fracture toughness increased to a maximum value and then decreased [98].

2.4.5.2 Resonant Ultrasound Spectroscopy

A method outlined by Migliori et al. has also proven valuable in non-destructive testing of materials [99]. Resonant ultrasound spectroscopy (RUS) can provide a complete elastic constant matrix of a material. This provides data for the determination of Poisson's ratio, in addition to the anisotropy of a material. Ren et al. used the RUS method in combination with Vickers microindentation and nanoindentation and biaxial flexure testing to characterize PbTe-based TE materials [100]. With the combination of these tests, Ren was able to determine Young's modulus, shear modulus, Poisson's radio, hardness and fracture strength of the material, providing a complete picture of the sample's mechanical response.

3 EXPERIMENTAL DETAILS

3.1 Sample Preparation

Elemental powders of Zr, Ni and Sn with purity greater than 99 wt% were used as starting materials. Mechanical alloying was performed in a Spex CertiPrep 8000M Mixer/Mill using a hardened steel vial and balls. The powders were combined (stoichiometric ratio of 1:1:1) under an argon atmosphere and sealed within a vial. The air tight seal is maintained by a rubber o-ring that sets in the cap of the vial. Initial powder mass of 6 grams of the elemental powders mixture were added to each vial providing a ball to powder mass ratio of about 3.5:1. This ratio was set based on trial and error for obtaining the proper amount of post milling yield, but still allowing the alloying reaction to take place quickly. Samples were milled under argon atmosphere. Excessive heating was controlled by circulating air through the mill with electronic fan. Samples were opened under normal atmosphere and loose powder was collected into vials. About 2.5-3 grams of powder were recovered for each sample due to caking on the sides of the vial and the balls.

Samples were consolidated by hot press (HP) or Spark Plasma Sintering (SPS). HP samples were heated to a temperature of 850 °C and held for 60 minutes, and remained under a uniaxial pressure of 100 MPa for 180 minutes. SPS samples were internally heated by a DC current to a temperature of 825 °C and held for 7 min, until thermal expansion was observed and consolidated under a dynamic vacuum of less than 2 Pa. Densities of samples were calculated based on their geometry after consolidation. Calculated density was compared with theoretical density obtained from JCPDS reference pattern 23-1281. [101]

3.2 Spex 8000M Mixer/Mill

Spex 8000M Mixer/Mill is capable of handling moderate amounts of a sample for grinding or pulverizing. The equipment used is shown in Figure 3.1. Maximum capacity for grinding is about 25 mL. Mechanical alloying requires a smaller amount of sample to maximize number of impacts for each grain of powder. Hardened steel vials were chosen as they have a higher Mohs hardness than each of the constituent powders. Mohs hardness characterizes the ability of one material to scratch another. A material with a larger Mohs hardness indicates resistance to scratching by a material with lower Mohs hardness.

Figure 3.1: Mixer Mill and Hardened Steel Vial

3.3 Sample Analysis

Collected powder was characterized by X-ray diffraction with a Panalytical X'Pert Pro system using Cu Kα radiation at an operating voltage of 45 kV and current of 40 mA. Continuous scans were performed in standard Bragg-Bretano ($\theta - 2\theta$) mode from 25° to 80° 2θ with a 0.05° step size and a counting time of 25 seconds/step.

Crystallite size and lattice strain were estimated using the Williamson-Hall method [81] to separate size and strain broadening of the diffractions lines from the XRD data using the equation:

$$B_{sam}\cos\theta = \frac{0.9\lambda}{Size} + 4\cdot(Strain)\cdot\sin\theta \qquad (3.1)$$

where B_{sam} is the full width of the line at half maximum intensity (FWHM) in radians, corrected for instrumental broadening, λ is the wavelength of the X-ray, and θ is the Bragg angle for the XRD line. The instrumental broadening was determined by measuring the FWHM of a sample of ZrNiSn that was synthesized by high temperature synthesis, similar to the methods described by [49] and [66].

Thermal diffusivity was measured and specific heat capacity was estimated under nitrogen atmosphere up to a temperature of 775 K with laser flash analysis using a NETZSCH LFA 457 Microflash instrument. Seebeck coefficient and electrical resistivity were measured under a helium atmosphere up to a temperature of 775 K using a ZEM-3, a combination Seebeck Coefficient/Electrical Resistance Measuring System manufactured by Ulvac Technologies.

3.4 The X'Pert Pro System

This section describes the X'Pert Pro System used in this research. Details were obtained from the system manual [102].

Figure 3.2: PW 3040/60 X'Pert Pro X-ray Diffraction System (from [102])

The Philips X'Pert PRO X-ray diffraction system can perform a wide variety of applications in X-ray diffraction.

The following applications are possible with the X'Pert diffractometer:

- Quantitative phase analysis of batches of samples
- Crystallography and Rietveld analysis on samples with flat or irregular surfaces
- In-Plane diffraction on thin films
- Residual stress analysis of flat samples or irregularly shaped materials
- Phase analysis of samples with flat or irregular surfaces; of thin films, and of samples in glass capillaries
- Texture analysis on all kinds of materials with preferred orientation of the crystallites

The X'Pert PRO system is able to handle a variety of optical and sample handling accessories by use of the PreFIX concept. PreFIX stands for: Pre-aligned Fast Interchangeable X-ray modules. The modules and accessories are factory aligned, and easily dismounted and then mounted to the system again with out needing additional alignment. The versatility of the X'Pert PRO system is realized by combining the optics and sample holders in different arrangements. The X'Pert PRO system is run on Windows operating system.

The X'Pert PRO X-ray Diffraction system is comprised of the following:

- Goniometer; the central part of the diffractometer, it controls and measures the angles of the incident and diffracted beam optics
- X-ray tube; mounted on the goniometer in a tube shield
- Incident beam optics and diffracted beam optics
- Sample stage
- Detector

3.4.1 Goniometer

The goniometer used in this research is a 2 axis system with 2θ and θ the variables. There is no travel in the ϕ (around normal to sample stage) or ψ (tilt about the horizontal plane) directions. θ is the angle between the incident beam and the sample surface while 2θ is the angle between the incident beam and the diffracted beam. In this configuration θ and 2θ can be adjusted independently of one another. The goniometer has minimum θ and 2θ step sizes of 0.0001° and maximum step sizes of 1.27°. The angular range of θ is -20° to 120° and of 2θ: -40° to 170°. The radius of the goniometer is 240 mm.

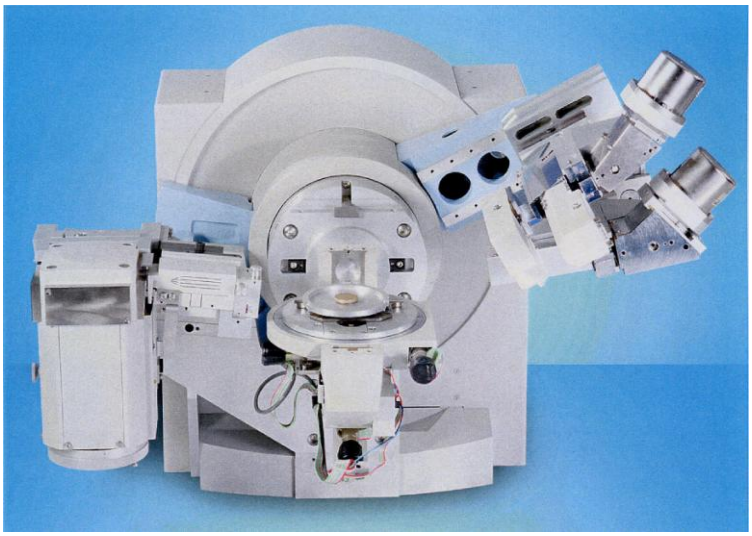

Figure 3.3: X'Pert PRO MPD θ - 2θ System (from [102])

3.4.2 X-ray Source

The x-ray source used in the X'Pert PRO system is a high power ceramic filament tube with a Cu-target. Current is passed through the filament, electrons are thermally emitted, and accelerated towards the anode by the high voltage potential. The electrons striking the anode produce X-rays which exit through beryllium windows. Due to the excessive heat produced by the X-ray production, the anode is also cooled. The tungsten filament has a maximum power rating of 2.2 kW, maximum voltage of 60 kV and maximum current of 60 mA. Normal operating values are 40 kV and 45 mA. Cu gives a K_α of 1.542 Å and K_β of 1.3922 Å. Cu is the most common material used for normal powder diffraction work, phase identification and quantitative analysis

Figure 3.4: Ceramic Diffraction X-ray Tube (from [102])

3.4.3 Incident Beam Optics

After leaving the X-ray tube, the beam passes through the incident beam optics before striking the sample. The incident beam optics control the size and divergence of the beam.

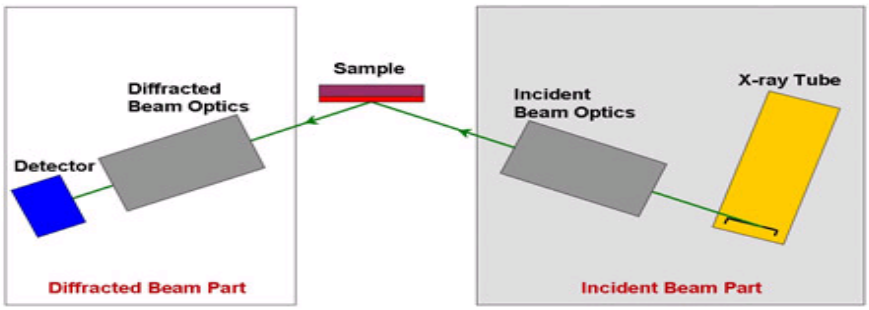

Figure 3.5: X-ray beam bath (from [102])

3.4.3.1 Programmable Divergence Slit (PDS):

Divergence slits are fitted in the incident beam path to control the equatorial divergence of the incident beam. This directly influences the amount of the sample that is irradiated by the beam. The divergence slit is controlled by software and allows for either a fixed angular divergence or a fixed irradiated length so that the angular divergence changes as a function of θ. The PDS module contains a slot for Soller slit and a beam mask.

All measurements in this research were made with a fixed divergence of 1/4°.

3.4.3.2 Incident Beam Mask

Beam masks are used to control the irradiated width on the sample. They are installed on the PDS, accepted by the beam mask holder. X'Pert PRO comes with multiple beam masks of 5, 10, 15, and 20. For this research, 15 mm is used.

Figure 3.6: Incident Beam Masks (from [102])

3.4.3.3 Soller Slits

Soller slits control the axial divergence of the X-ray beam. The X-ray source radiates both above and below the plane of incidence, so a Soller slits can remove much of this divergence. It consists of a series of parallel plate between which the X-rays must pass (shown in the figure below). Soller slits improve the peak shape and the resolution for a 2θ type scan. A 0.04 rad Soller slit is used in this research.

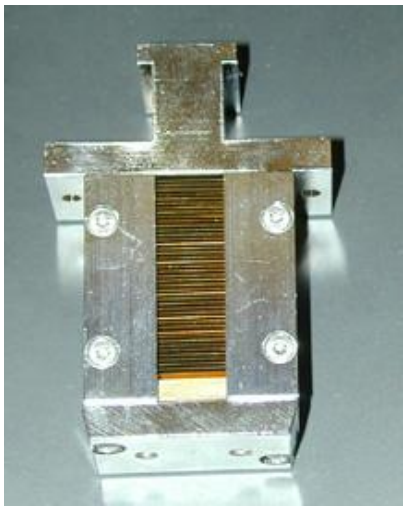

Figure 3.7: Soller slit (from [102])

3.4.4 Diffracted Beam Optics

After the X-ray strikes the sample they pass through the secondary, or diffracted beam, optics before they strike the detector. These components often consist of programmable receiving slits, Soller slits, fixed anti-scatter slit, and monochromators. This research used all of these components.

3.4.4.1 Programmable Receiving Slit (PRS)

A PRS is similar to the previously described PDS. It provides a defined receiving slit height that can be varied from 0.01 mm to 3.0 mm in steps of 0.01 mm. In addition it serves as a mounting area for the other components of the diffracted beam optics. A slit receiving height of 0.3 mm was used in this research.

Figure 3.8: Programmable Receiving Slit (from [102])

3.4.4.2 Fixed Anti-Scatter Slit (FASS)

Anti-scatter slits are used to control the amount of diffracted X-ray beam that is accepted by the detector. In parallel beam geometry, the combination of an anti-scatter slit and a receiving slit can be used instead of a parallel plate collimator. The FASS is mounted directly onto the PRS. The FASS used in this research is 1/4°, the others available are 4°, 2°, 1° and 1/4°.

3.4.4.3 Soller Slit

Similar to the Soller slit that controls the divergence from the incident beam optics, an additional Soller slit controls the acceptance of the diffracted beam. The Soller slit is mounted directly onto the PRS. A Soller slit of 0.04 radians is uses in this research with the diffracted beam optics.

3.4.4.4 Curved Crystal Monochromator

Diffracted beam monochromators are situated before the X-ray detector. They are used to reduce the background radiation, eliminate unwanted lines and reduce sample fluorescence. The curved crystal monochromator used in this research helps focus the beam. The curvature of the crystal is such that the crystal surface, the receiving slit and the detector slit all lie on the focusing circle of the monochromator.

3.4.5 Detector

Figure 3.9: Proportional Detector (from [102])

After the X-ray beam passes through the diffracted beam optics, it enters the detector. The detector counts the number of photons, and measures the intensity of the X-ray beam as a function of the 2θ position of the goniometer. The detector used in this research is a sealed proportional detector. The detector has a window size of 20 x 24 mm^2, has Cu Kα efficiency of 84%, energy resolution of 19%, and maximum count rate of 1000 kcps. The detector has a 99% linearity range during counting.

3.4.6 Sample Platform

Sample platforms are the components the place the sample at the correct height and distance from both the X-ray source and the detector. In this research the powder samples were sprinkled on a circular low-background filter and then mounted into the circular PW18xx, sample holders. These samples holders were held by the PW3072/60 sample stage, which was mounted directly onto the goniometer and is shown in Figure 3.10. The samples stage uses a spring-loaded lever that pressed the sample holder to the proper reference plane. Due to the spring-loading, the sample mass cannot exceed 150 g, or it will overcome the spring force and not remain at the correct reference plane.

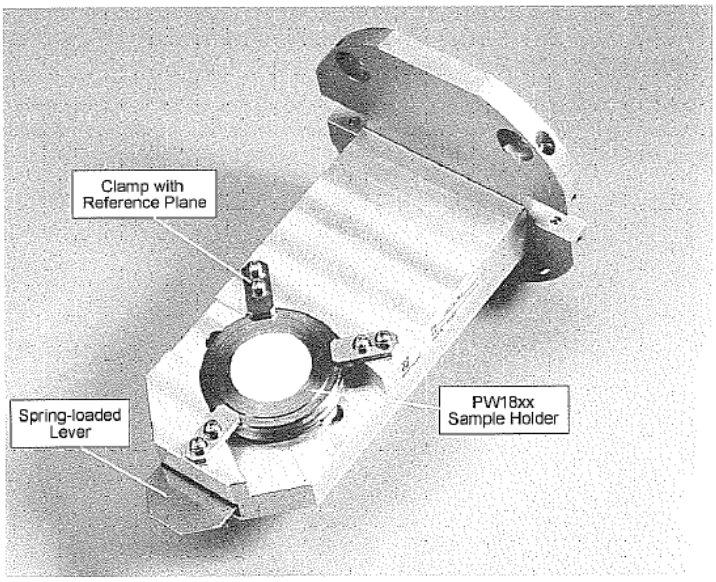

Figure 3.10: PW3072/60 Stationary Stage for PW18xx Sample Holders (from [102])

3.5 Microindentation and Nanoindentation

Hardness was measured by microindentation technique using a Shimadzu Micro Hardness Tester HMV-2 Series with a Vickers indentation tip. Twenty-five indentations (5 x 5 array with 100 μm spacing between indents) with a load of 0.49 N were made in each specimen. Load chosen was the largest load that did not produce cracking in the sample. Resulting impressions were optically measured using Newage Testing Instruments Computer Assisted Measurement software package. Each indent was evaluated for cracking and symmetry and rejected if there was excessive deformation. Hardness was calculated with the standard formula:

$$H = \frac{P}{A} \tag{3.2}$$

where P is the applied load and A is the projected area. Substituting for projected area based on Vickers indenter geometry, equation 3.2 is changed to incorporate the average length of the diagonal, d, of a Vickers indent:

$$H = \frac{2P}{d^2} \tag{3.3}$$

This is slightly different from the standard formula for Vickers hardness which is based on the contact area and the load measured in kilograms-force. In this case Vickers hardness is expressed in units of HV (hardness Vickers). In contrast, Equation 3.3 is in used in this work because it parallels the method used to calculate the hardness by nanoindentation described below. P is force, measured in newtons [N], A is projected area and H is measured in pascals

[Pa], which is directly comparable to the hardness value determined by the nanoindentation, also measured in pascals.

Elastic modulus and hardness were measured as a function of depth by nanoindentation using the Agilent G200 Nano Indenter. Twenty five indentations (5 x 5 array with 50 μm spacing between indents) up to a fixed maximum depth of 2000 nm were made on each specimen. Hardness and elastic modulus were calculated from a commercial software package [103]. In addition to the 5 x 5 array using the continuous stiffness measurement method, a 3 x 3 array of indents using the basic method, up to a maximum depth of 2000 nm, was made to rule out any effects of pile up [90].

3.5.1 Agilent Standard G200 System

The G200 is a universal testing system that delivers high performance and the ability to customize tests. The complete G200 system is shown in figure 3.11. The TestWorks 4 software package is used to collect, analyze and export data from the G200 unit.

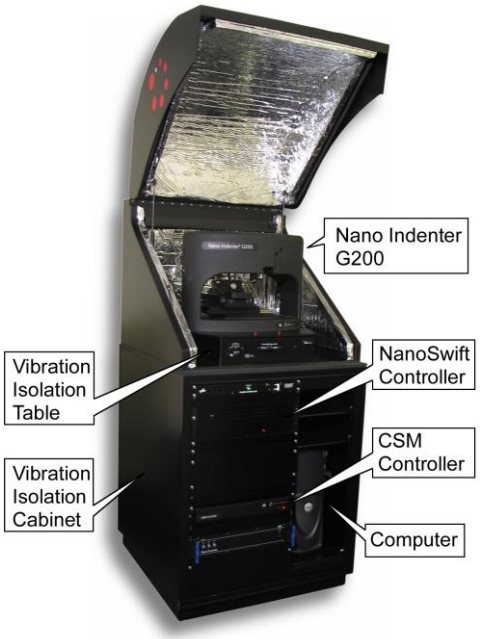

Figure 3.11: The Standard G200 System (from [113])

3.5.1.1 Nano Indenter G200

The Nano Indenter G200 sits upon a vibration isolation table and holds a sample tray mounted on an automated stage. The sample tray consists of 4 vacant spots for samples. The fifth, center spot, is for the reference sample and is not removed.

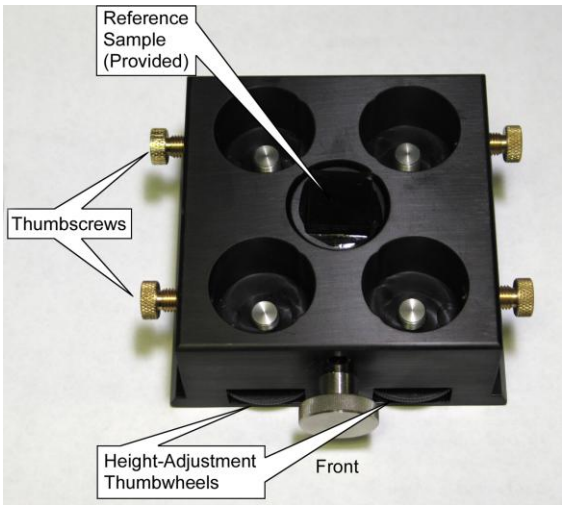

Figure 3.12: The sample Tray (from [113])

A set of indents that is carried out consecutively is called a batch, within a batch multiple samples can be indented, each with a different test procedure (method). The system is automated, so after test sites are chosen, the tests will run to completion.

3.5.1.2 Indenter

The G200 can accept different types of tips for different applications. The most common tip used, and the tip used in this research, is a diamond Berkovich indenter. Shown in Figure 3.13, the Berkovich indenter is a three-sided pyramid with total included angle of 142.3 ° and a half angle of 65.35 °. The three-sided geometry allows for ease in grinding the tip to a fine point, which is desirable for indentation applications.

Figure 3.13: Diamond Indenter with Berkovich Geometry (from [113])

3.5.1.3 Physics of Instrumentation

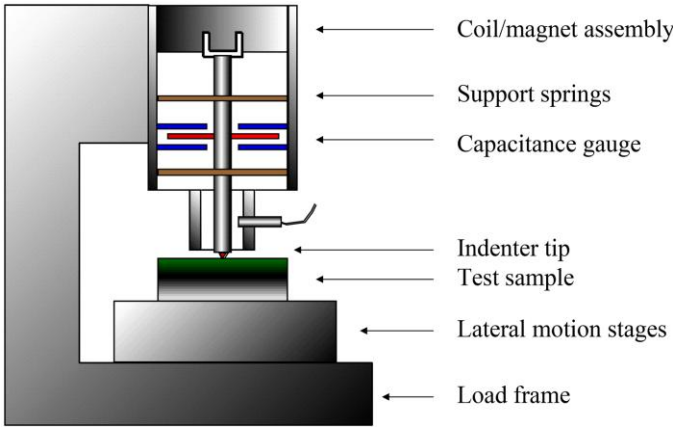

Figure 3.14: Schematic of the Nano Indenter G200 (from [113])

Test sites are chosen with an optical microscope, the sample is then translated to the indenter and the tests are performed at the desired locations. The lateral motion states are piezo-driven and have accuracy of about 1.5 μm. Force is generated by the coil/magnet assembly. The force on the indenter shaft is directly proportional to the current passed through the coil. This assembly was initially calibrated at the factory using the indenter to balance a series of weights. Displacement sensing is accomplished by the three plate capacitive arrangement shown in Figure 3.14. The two outside plates are fixed to the head and have holes in the center to accommodate the indenter shaft. The center plate is fixed the indenter shaft and is can move vertically between the two outside plates. The position of the indenter column within the gap is determined by observing the difference in voltage between the center plate and either of the two outside plates. The displacement sensor is calibrated using laser interferometry and has theoretical resolution of <0.01 nm. This plate and indenter assembly is supported by two leaf springs, which are designed to have low stiffness in the vertical direction and high stiffness in the horizontal direction.

3.5.1.4 Theory

Instrumented-indentation testing (ITT) employs a high-resolution actuator to force an indenter into a test surface and a high-resolution sensor to measure the resulting penetration. Using this technique, the contact area under load can be inferred from the load-displacement data. As the indenter is driven into the material, both elastic and plastic deformation cause the formation of a hardness impression conforming to the shape of the indenter to some contact depth h_c. A typical load-displacement curve is shown in Figure 3.15, where $S = dP/dh$ and is known as the elastic stiffness of the contact.

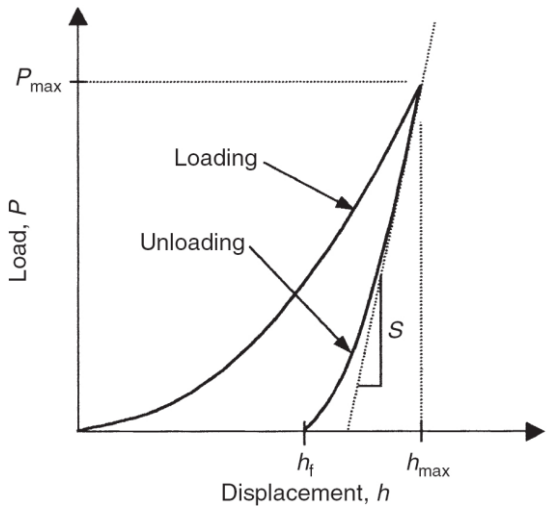

Figure 3.15: Typical load-displacement curve for ITT (from [113])

Hardness of the sample is determined by equation 3.2, by the same method used for microhardness evaluation. In this case, however, the projected contact area A is a function of the contact depth h_c.

$$A = f(h_c) \tag{3.4}$$

The area function is an empirical relationship specific to the indenter tip being used. Over time, due to repeated use, the tip will dull and a new area function is determined by calibration.

Elastic modulus of the sample, E, is determined from the reduced modulus, E_r, given by:

$$E_r = \frac{(\sqrt{\pi} \cdot S)}{2\beta\sqrt{A}} \tag{3.5}$$

Where A is the projected contact area (Eq. 3.4), S is the elastic stiffness of contact, and β is a constant that depends on the geometry of the indenter. For Berkovich indenters $\beta = 1.034$. The elastic modulus of the test material, E, is calculated using the expression:

$$\frac{1}{E_r} = \frac{(1-\nu^2)}{E} + \frac{(1-\nu_i{}^2)}{E_i} \tag{3.6}$$

Where ν is the Poisson's ratio for the test material and E_i and ν_i are the elastic modulus and Poisson's ratio, respectively, of the indenter. The Poisson's ratio of the test material, ν, is estimated and an error of ± 0.1 will produce about a 5% uncertainty in the calculated value of E.

4. RESULTS

4.1 ZrNiSn X-Ray Diffraction Data

Scans were performed over a 2θ range from 20° - 85° with a step size of 0.05° at 25 seconds per step for a total scan time of about 9 hours. Theses parameters were chosen to obtain a strong signal to background ratio and to encompass the appropriate area for phase identification. Low background, compared to peak height, provides a smooth peak shape, which allows for easier analysis of the FWHM.

X-ray powder diffraction measurements were made on ZrNiSn powders with ball milling times varying from 2 to 40 hours. The diffraction pattern for a sample milled four hours is shown in Figure 4.1. The pattern in Figure 4.1 has been treated using background removal and kα_2-stripping algorithms. A ZrNiSn half-Heusler alloy was formed and is identified by a comparison with the stick pattern of JCPDS reference pattern 23-1281 – NiSnZr (space group $\overline{F}43m$) [101]. Peaks are labeled with Miller indices based on this identification.

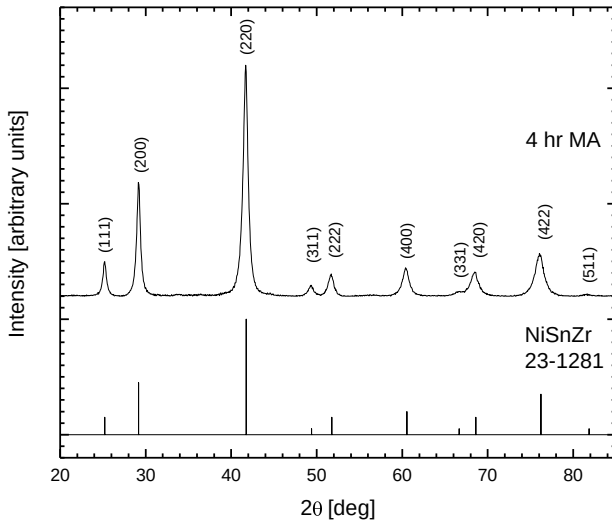

Figure 4.1: XRD pattern for MA ZrNiSn, ball milled for 4 hours, compared to stick patten of NiSnZr half-Heuser alloy standard.

Figure 4.2 shows raw XRD data collected from powders milled for various times. The ZrNiSn pattern is seen as early as 2 hours into the milling process. The 2 and 3 hour samples contain additional peaks that can be indexed as the most intense peaks of zirconium and nickel and are marked in the figure. The Zr and Ni peaks show broadening, indicatding that the remaining Zr and Ni has undergone grain refinement and an increase in lattice strain. At milling times of 10 hours and above, additional broad peaks appear at 34.1°, 39.4° and 56.8° 2θ. These peaks are marked with an x in the 40 hour pattern in Figure 4.2. They can be indexed as the (111), (200) and (220) peaks of a f.c.c. structure with lattice parameter of 4.56 Å. This is indicative of a solid solution formation. The most intense peak of 34.1° is visible in the 10 hour

milled sample. At 20 hours, all 3 peaks can be distinguished and they increase in size by 40 hours of milling.

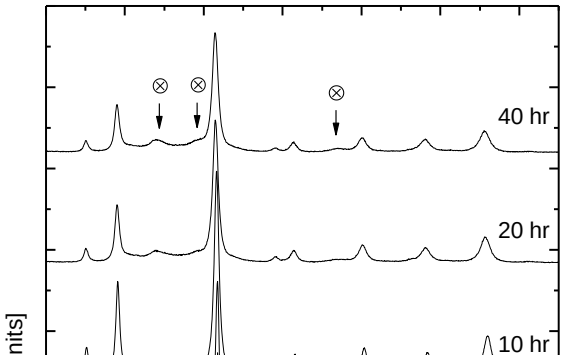

Figure 4.2: XRD patterns of mechanicallly alloyed ZrNiSn samples after miling times of 2 hours to 40 hours

The half-Heusler phase peaks broaden with increased milling time, which is typical of the MA process. The peak broadeing is due the the reduction in grain size and increase in lattice strain induced by continued milling. The crystallite size and lattice strain of the MA powders were extracted from the XRD data using the Williamson-Hall method as described in section 2.3 [81]. The following equation is used:

$$B_{sam}\cos\theta = \frac{0.9\lambda}{Size} + 4\cdot(Strain)\cdot\sin\theta \qquad (4.1)$$

Where B_{sam} is the FWHM in radians, corrected for insturmental broadening, λ is the X-ray wavelenght and θ is the Bragg diffraction angle for the XRD line. Each peak was plotted with $B_{sam}\cos\theta$ on the y-axis and $\sin\theta$ on the x-axis, the resulting stright line has a slope related to the strain and a y-intercept related to the crystallite size. Instramental broadening was obtained by using XRD to measure a sample of ZrNiSn with sufficiently large grain size such that any

broading of the sample is due to the insturment. Figure 4.3 shows the Williamson-Hall plot for a sample milled for 6 hours, with the data from each peak forming nearly a straight line.

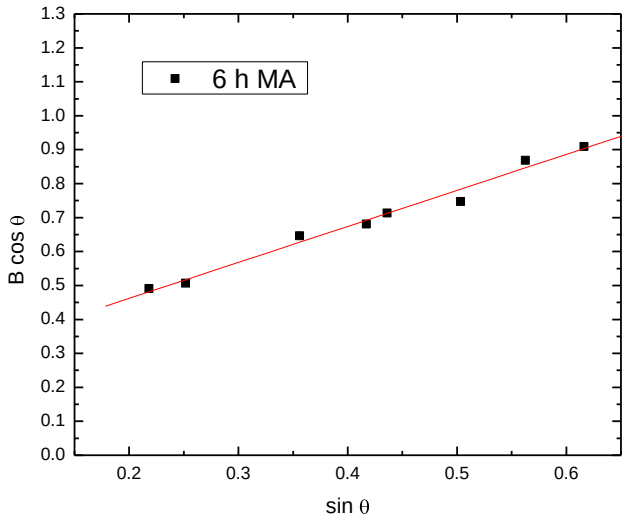

Figure 4.3: Williamson-Hall plot of largest peaks for ZrNiSn half-Heusler phase milled for 6 hours

A crystallite size and lattice strain value for each milled sample was obtained. These values are plotted in Figure 4.4 and are typical of MA results [104]. The minimum grain size of the ZrNiSn half-Heusler alloy is estimated to be less than 25 nm after 40 hours of milling. After about 4 – 6 hours, the grain size has reached 30 to 40 nm and does not undergo significant further reduction with increased milling time.

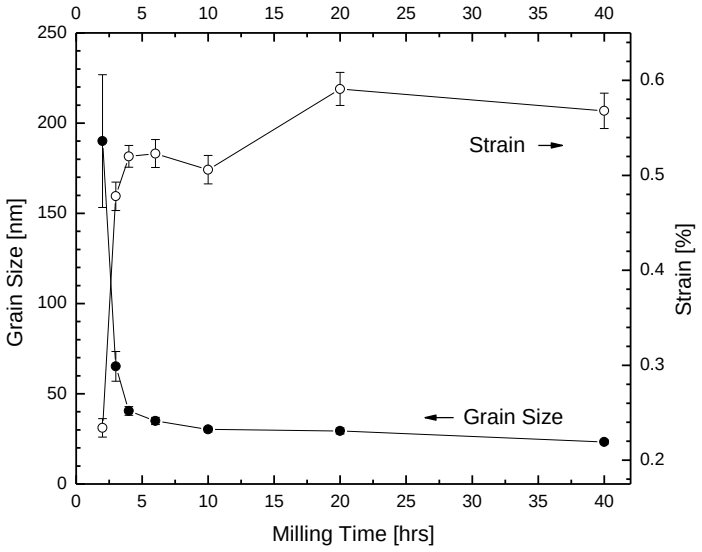

Figure 4.4: Grain size and strain as a function of milling time for mechanically alloyed ZrNiSn half-Heusler phase.

Broadening of the half-Heusler peaks is accompanied by a shift of the peaks to lower 2θ values at longer milling times suggesting an increase in lattice parameter. The lattice parameter for each pattern was obtained from a least squares fit to the experimentally determined peak positions using the equation:

$$a = \frac{\lambda}{2\sin\theta}\sqrt{h^2 + k^2 + l^2} \tag{4.2}$$

where *a* is the lattice parameter, *h, k,* and *l* are the Miller indices for a given peak, and θ is the Bragg diffraction angle. Figure 4.5 shows the change in lattice parameter $\left(\frac{\Delta a}{a_0}\right)$ as a function of milling time. For this compound, $a_0 = 6.113$ Å is the lattice parameter of the reference NiSnZr compound [101]. The estimated lattice parameter increases from 6.116 Å after 2 hours to 6.162 Å after 40 hours of milling. Slight increases in lattice parameter upon ball milling have been observed in other ordered intermetallic systems and have been attributed to anti-site disordering [104].

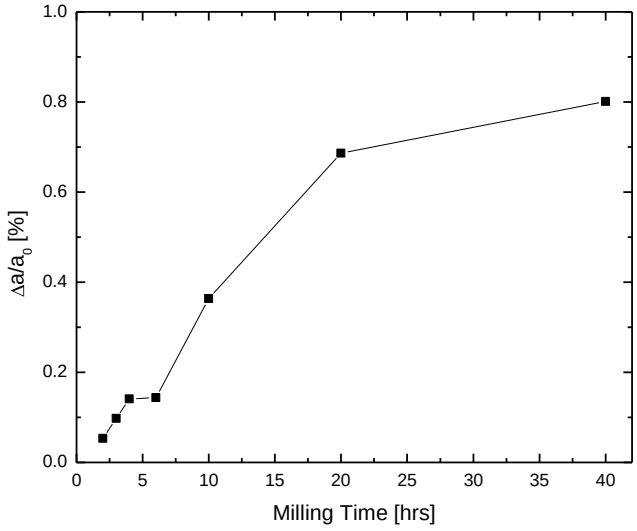

Figure 4.5: Percent change in lttice parameter as a function of milling time for mechanically alloyed ZrNiSn half-Heusler phase

4.2 Particle Size Measurements

BET measurements were used to approximate the specific surface area for the ball-milled powders. The specific surface area had a random variation between 1.7 and 3.0 m^2/g. If a spherical particle shape is assumed, this corresponds to an average particle size between 250 and 500 nm as shown in Table 4.1. Scanning Electron Microscope (SEM) images were taken of the ZrNiSn sample milled for 2 hours. The particle size results are consistant with the BET particle size estimate. An SEM image of the ZrNiSn sample milled for 2 hours is shown in Figure 4.6. The particle marked in the image is estimated to have a diameter of 317 nm. These results are consistant wth other particle size measurements for ball milling of brittle systems [110,111].

Table 4.1: Density meaured by gas pycnometer and specific surface area estimated by BET as a function of milling time.

Milling time (h)	**Density (g/cm^3)**	**Specific Surface Area (m^2/g)**
2	7.9491	1.731
3	7.9157	2.1122
4	7.9563	1.9055
6	7.9966	1.5177
10	8.1523	2.9703
20	8.0965	2.5044
40	8.0504	1.7389

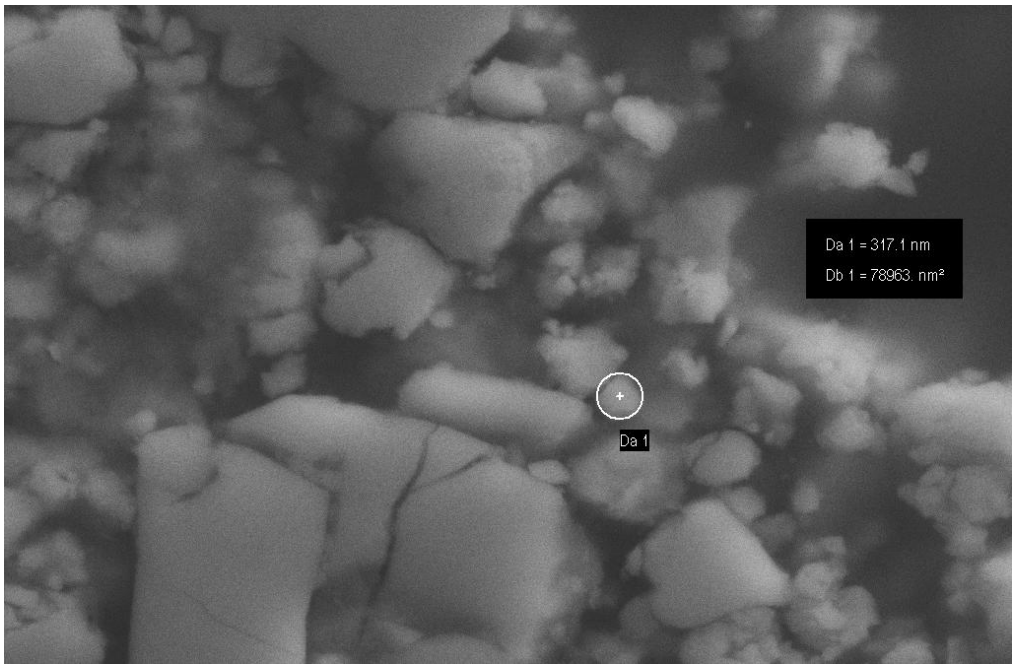

Figure 4.6: SEM image of a ZrNiSn half-Heusler alloy milled for 2 hours

4.3 Thermal Stability Analysis

Differential Scanning Calorimetry (DSC) measurements were taken at a heating rate of 20 °C/min from for each of the MA powders. The results are presented in Figure 4.7. The MA powders are compared to a powder mixture containing zirconium, nickel, and tin elemental powders. As can be seen in Figure 4.7, the mixture of elemental powders has an endothermic peak around 230 °C. This corresponds to the melting point of elemental tin at 232 °C. This feature is absent in the remaining DSC curves for the milled samples, indicating the elemental powders of Zr, Ni and Sn have formed a different phase. The data for the 2-hour ball milled sample has an exothermic peak at about 365 °C. A similar feature was also observed by Schulz et al. while studying the amorphization reaction in Ni-Zr alloys during mechanical alloying [105]. Shulz notes that, in addition to crystallite growth, strained Ni-Zr powders will undergo strain relaxation from about 350 °C to about 500 °C. This is consistent with the XRD pattern of the 2-hour milled sample (Figure 4.2), which shows broadened reflections of the remnants of Zr and Ni elemental powders and indicates highly strained crystallites of these phases. As a result, the DSC feature in the 2-hour milled sample, at 365 °C, is attributed to strain relaxation and recrystallization as in the study by Shulz et al. The feature disappears for samples milled longer than 2 hours, consistent with the XRD results showing the impurities disappear at longer milling times.

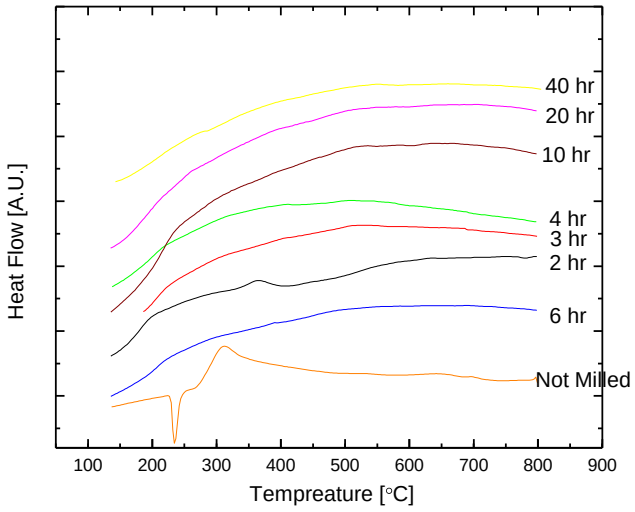

Figure 4.7: Differential Scanning Calorimetry measurements of ZrNiSn half-Heusler phase, labeled by their milling time and elemental Zr, Ni, and Sn, which was not milled.

The absence or endothermic peaks in the DSC curves for samples milled longer than 2 hours demonstrates that a stable half-Heusler alloy has formed. This is consistent with the thermal analysis competed by Shen et al., where he noted that the only endothermic peaks for a ZrNiSn sample form at about 810 °C, due to a peritectic reaction of ZrNiSn with a liquid phase caused by the impurities, and at about 1030°C, which is identified as the melting point of ZrNiSn [66]. Also of note: there is a slight variation in the shape of the 4-hour milled sample as it appears to have a different slope during its initial heating cycle. This indicates that the 4-hour sample experienced a difference in temperature with the alumina reference sample that changed at a different rate than the other MA powder samples. A possible explanation is the mass of the sample used for the DSC. The 4-hour sample contained the smallest mass of all the samples, measured at 12 mg. The second smallest mass was 14.8 mg for the 3-hour sample. Another possible explanation for the shape of the DSC curve for the 4 hour sample is the presence of gas contaminants that were not completely evacuated before sealing the tube. The 3-hour sample DSC curve is slightly shorter than the others because the thermal analysis unit was at a higher temperature when the cycle began.

4.4 Consolidation of Sample

ZrNiSn alloys milled for 6 hours were chosen as candidates for thermoelectric analysis due to the small grain size obtained by MA and the lack of the appearance by the f.c.c. solid solution phases present at longer milling times. Samples were consolidated by hot pressing (HP) and by spark plasma sintering (SPS) as discussed in section 3.1. The XRD patterns of the HP and SPS samples are shown in Figure 4.8. After consolidation the peaks narrow due to strain relaxation and grain growth. Lattice strain and grain growth are estimated by using the Williamson-Hall method discussed in section 4.1 and results are tabulated in Table 4.2. Both consolidation methods induce a grain growth with grains in the SPS sample growing only 8%.

In addition, the lattice strain for the SPS sample nearly disappears, indicating that the high temperature was able to relax the strain but the short SPS heating cycle did not induce excessive grain growth. Both samples remain in the nano-scale crystallite size regime. Before measurement the HP sample had to be sanded to remove remaining graphite from lubrication during hot pressing. This grinding process may have caused additional strain, noted by only a 63% reduction in Table 4.2 for the HP sample. Mechanical grinding has been shown to induce lattice strain [106].

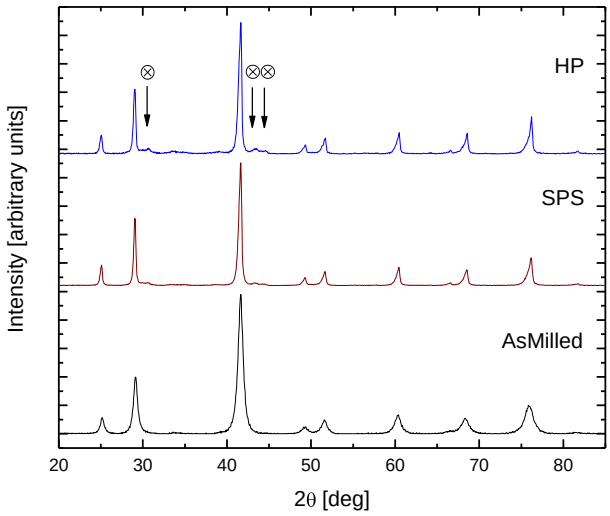

Figure 4.8: XRD patterns of ZrNiSn consolidated by different methods

In both pressed samples additional peaks appear near 30.8°, 43.5° and 44.5°. These peaks are marked in Figure 8 and can be indexed as the most intense peaks ((101), (102), and (110)) of Ni_3Sn_2. The half-Heusler phase dominates the HP and SPS XRD patterns, indicating that the impurities will have minimal effect on the transport properties of the sample.

Table 4.1: Grain size and lattice strain of ZrNiSn samples, milled for 6 hours and consolidated by SPS or HP

Sample	Grain Size (nm)	Percent Change	Lattice Strain (%)	Percent Change
HP	43	19%	0.19	-63%
SPS	39	8%	0.026	-95%

4.5 Summary of Synthesis

A ZrNiSn half-Heusler alloy was successfully synthesized by MA. The half-Heusler phase dominates the XRD spectrum at 2 hours and phase purity increases with further milling. Further milling produces grain refinement and increase in lattice strain, which is demonstrated by broadening of reflection peaks in the XRD pattern. Crystallite size is estimated to reach 25 nm

after 40 hours of milling but is accompanied by a transformation into a solid solution. F.c.c. solid solution peaks appear after about 10 hours of milling.

4.6 Thermoelectric Properties

Thermoelectric properties were evaluated in the temperature range of room temperature up to 775 K. This temperature range is chosen as it is a possible application range for these thermoelectric materials. For example, to recover waste heat from a vehicle, the likely operating temperature will be from 450 K to 725 K. With this consideration, a high figure of merit in this range is desirable.

Electrical resistivity is shown in Figure 9. The electrical resistivity decreases with increasing temperature, which is typical of a semiconductor. The resistivity of the MA system is lower than the previously reported value for a high temperature synthesis ZrNiSn system but does not reach the lowest electrical resistivity achieved by doping the system with Sb [48,53]. Doping with Sb adds electrons and gives the compound a more metallic like behavior, which drastically reduces the electrical resistivity. The lower resistivity of the HP sample may be attributed to the length of time that the sample was pressed during its high temperature phase, allowing greater contact area between the individual grains.

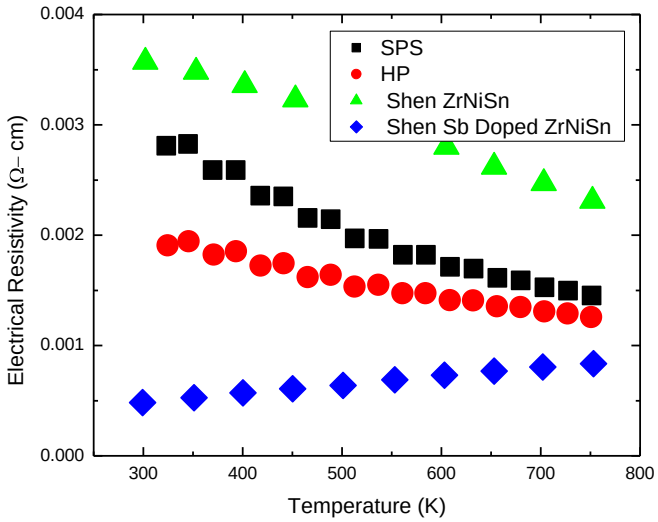

Figure 4.9: Temperature dependence of the electrical resistivity of HP and SPS samples compared with high temperature synthesis ZrNiSn and Sb doped ZrNiSn from Shen et al. [53]

Figure 4.10 shows the temperature dependence of the Seebeck coefficient for the HP and SPS samples compared with the previously reported result by Shen et al. [53]. SPS produces a larger $|S|$ than the HP sample, which can be attributed to the purity of the SPS sample, demonstrated by the XRD data in Figure 8. The HP sample has slightly larger ratio of impurity peaks to half-Heusler peaks than does the SPS sample. Neither sample reproduces the largest $|S|$

values achieved in literature. Both the HP and SPS samples show some peaks of Ni_3Sn_2, which appear to disrupt the half-Heusler phase and its transport properties.

Thermal conductivity of HP and SPS samples were measured as a function of temperature and are presented in Figure 4.11. For the HP sample, thermal conductivity remains between 6.0 W/m-K and 7.7 W/m-K for the entire temperature range. The SPS sample thermal conductivity remains between 5 W/m-K and 6 W/m-K. These ranges are lower than the previously reported values, as shown in Figure 4.11 [53]. The reduction in thermal conductivity is a result of a reduction lattice thermal conductivity due to smaller grain size and increased number of grain boundaries per unit volume. The driving force of lattice thermal conductivity is phonon transport, which is disrupted at the grain boundaries [57]. Figure 11 also verifies the smaller grain size produced by the SPS sample, compared to the HP sample reduces thermal conductivity. It has also been documented that consolidation by SPS seems to produce better transport properties than HP methods [69]

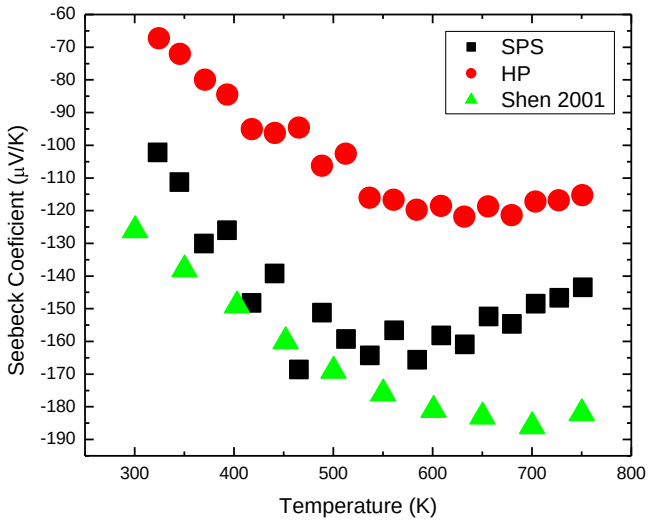

Figure 4.10: Temperature dependence of the Seebeck coefficient of HP and SPS samples compared with high temperature synthesis ZrNiSn from Shen et al. [53]

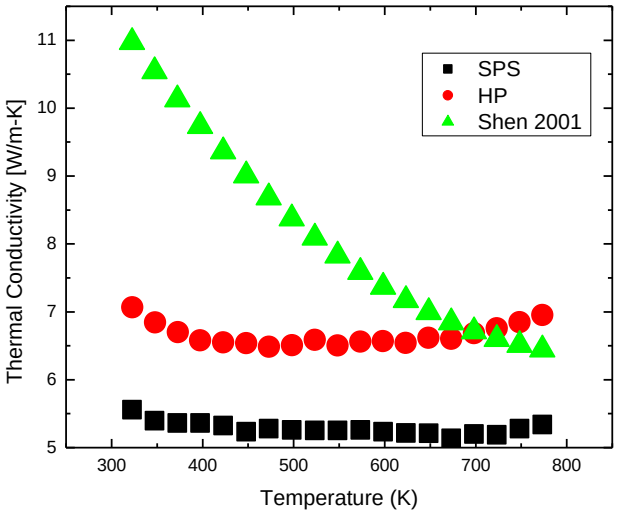

Figure 4.11: Temperature dependence of thermal conductivity of HP and SPS samples compared with high temperature synthesis ZrNiSn from Shen et al. [53]

Combining the data from figures 4.9, 4.10, and 4.11 yields the data for the dimensionless figure of merit, ZT. The temperature dependence of the figure of merit is displayed in Figure 4.12. This base system of ZrNiSn, without any dopants, achieves a maximum ZT of about 0.2 nearing 775 K. This value is in line with previously reported values of ZT for ZrNiSn alloys, but it is obtained at a lower temperature. Shen et al. reports high temperature synthesis ZrNiSn obtains a ZT of 0.2 at about 900 K. The SPS sample demonstrates a larger ZT than the HP and high temperature synthesis samples at all temperatures evaluated. The HP sample did not perform as well due to the lower Seebeck coefficient and the larger thermal conductivity over the measured temperature range.

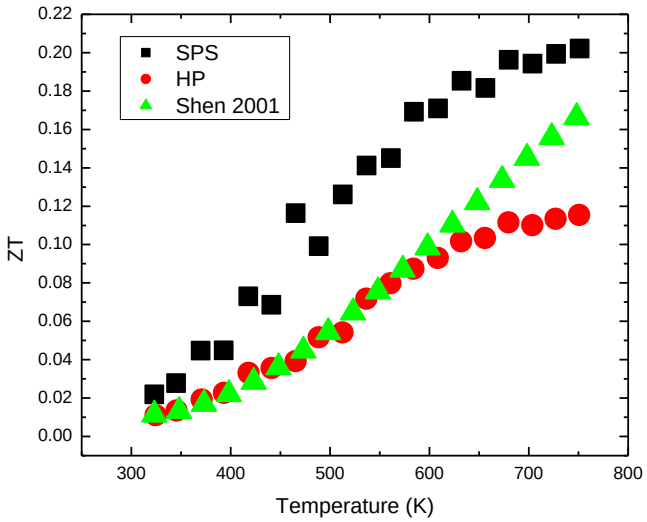

Figure 4.12: Temperature dependence of the figure of merit, ZT, of HP and SPS samples compared with high temperature synthesis ZrNiSn from Shen et al. [53]

4.7 Elastic Modulus and Hardness Measurements

Elastic modulus and hardness of both the HP and SPS sample were investigated using depth sensing indentation techniques. Hardness was confirmed with microindentation. The elastic modulus and harness were measured as a function of distance from the surface of the sample up to a distance of 1600 nm. The results are presented in Figure 4.13. The HP samples demonstrate a higher hardness and modulus of elasticity than the SPS samples, likely due to the synthesis method. The mean values for the elastic modulus and hardness of the SPS sample are 223.485 ± 2.673 GPa and 13.612 ± 0.329 GPa respectively. The mean values for the elastic modulus and hardness of the HP sample are 241.111 ± 4.027 GPa and 14.377 ± 0.594 GPa, respectively. Each of the 25 tests completed on both samples produce a calculated modulus and hardness over the specified 400 nm – 1600 nm calculation range. Each of the 25 values obtained by the tests is averaged into a single value with a standard deviation for each sample. The standard deviations for these measurements are small, indicating homogeneity of both samples.

In addition to the statistical standard deviation that results from the average hardness or elastic modulus of all 25 tests, each individual test can be examined to find the spread about its average. When examined over the same calculation range of 400-1600 nm, the standard deviation of each test is less than the standard deviation of the average of all tests. Theses results are shown below in Figure 4.14 for the standard deviation of the hardness of the HP and SPS samples for specific chosen tests. Because the standard deviation of each individual test is less than the statistical standard deviation calculated from averaging all tests, the statistical standard deviation of all tests is more representative of the spread in the data.

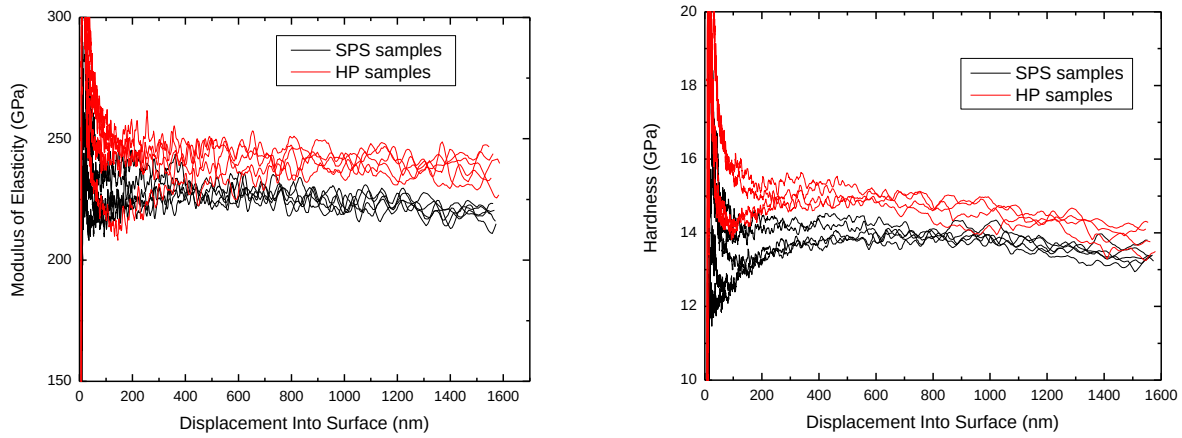

Figure 4.13: Elastic Modulus as a function of depth into sample surface for ZrNiSn alloy consolidated by HP and SPS

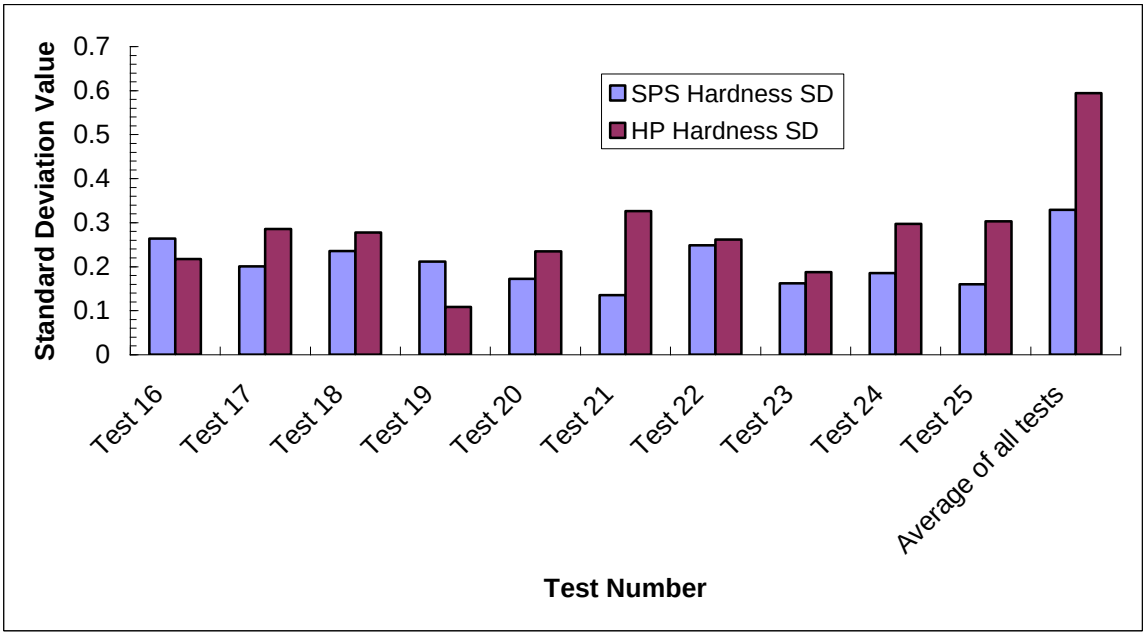

Figure 4.14: Standard deviation values of hardness for individual indentation tests on HP and SPS samples in calculation range 400 nm – 1600 nm

Microhardness test confirm that the HP sample demonstrates higher hardness than the SPS sample. Two indents are compared side by side below in Figure 4.15 for the HP and SPS sample. Both indents were made at the same load, but the difference in size is difficult to see by inspection alone. Measurement confirms that the HP sample's indents are slightly smaller than the SPS samples indents. The Vickers hardness value, measured in gigapascals, for the HP and SPS sample are 14.15 GPa and 13.69 GPa respectively. These values are compared with the nanoindentation hardness values in Figure 4.16 and show good agreement.

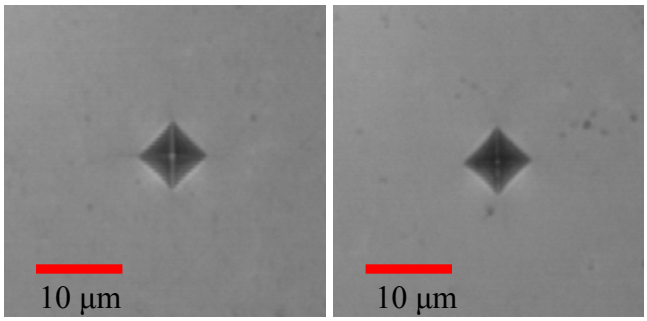

Figure 4.15: Microindentation of ZrNiSn half-Heusler alloy: HP sample (left) and SPS sample (right)

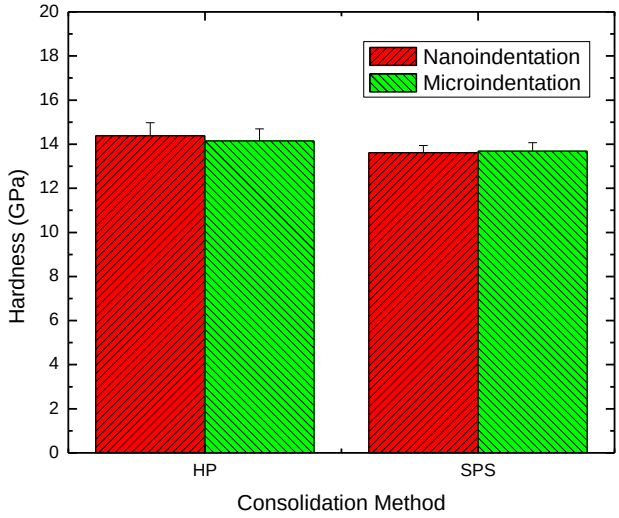

Figure 4.16: Nanoindentation values compared with Microindentation values for ZrNiSn half-Heusler alloy consolidated by HP and SPS.

5. CONCLUSIONS

A ZrNiSn half-Heusler alloy was successfully synthesized by mechanically alloying elemental powders. The half-Heusler alloy is well formed after 2 hours of milling but contains remnant Zr and Ni peaks. After 4 hours of milling, remnant peaks are not observed. The crystallite size of the ZrNiSn alloy is observed to decrease with increased milling time. After 40 hours of milling crystallite size reaches 25 nm. In addition to grain refinement, an increase in lattice parameter due to anti-site disorder is observed with increased milling time. After about 10 hours of milling, additional peaks form in the XRD spectrum and ZrNiSn is observed to undergo a transformation into a disordered crystalline phase – an f.c.c. solid solution. With increased milling time these peaks increase in size in comparison with the half-Heusler peaks.

A ZrNiSn half-Heusler thermoelectric compound was successfully consolidated by SPS and HP. Mechanical alloying reduced the grain size and consolidation methods attempted to minimize the grain growth during densification. The MA SPS ZrNiSn system shows a reduction in lattice thermal conductivity due to increased phonon scattering at grain boundaries caused by small crystallite size. Figure of merit of the MA SPS ZrNiSn sample shows improvement over previously reported values for base ZrNiSn system but does not reach values attained by doped ZrNiSn systems. Further improvements may be realized by increasing the Seebeck coefficient by improving the ordered structure of the sample with a heating cycle. Doing so, however, may eliminate the small grain size attained by MA. Mechanical alloying of a doped system may also yield improvements in thermoelectric performance by introducing additional mass based phonon scattering centers to reduce thermal conductivity while adding an electron to improve the electrical conductivity of the sample.

REFERENCES

[1] Lawrence Livermore National Laboratory, *U.S. Energy Flowchart 2008,* (2008)

[2] C. Suryanarayana, "Mechanical alloying and milling," *Progress in Materials Science, 46*, pp. 1-184, 2001

[3] J. S. Benjamin, "Dispersion strengthened superalloys by mechanical alloying," *Metallurgical and Materials Transitions*, vol. 1, p. 2943, 1970.

[4] J. S. Benjamin and P. S. Gilman, "Mechanical alloying," *Annual Review of Materials Research*, vol. 13, p. 279, 1983.

[5] P. Y. Lee, J. L. Yang, and H. M. Lin, "Amorphization behaviors in mechanically alloyed Ni-Ta powders," *Journal of Materials Science*, vol. 33, pp. 235-239, 1998.

[6] C. C. Koch, "The synthesis and structure of nanocrystalline materials produced by mechanical attrition: a review," *Nanostructured Materials*, vol. 2, pp. 109-129, 1993.

[7] M. Zakeri and M. Allahkarami and Gh. Kavei and A. Khanmohammadian and M. R. Rahimipour, "Synthesis of nanocrystalline Bi(2)Te(3) via mechanical alloying," *Journal of Materials Processing Technology*, vol. 209, pp. 96-101, 2009.

[8] J. S. Benjamin and T. E. Volin, "The mechanism of mechanical alloying," *Metallurgical and Materials Transitions B*, vol. 5, p. 1929, 1974.

[9] P. Lee and C. Koch, "Formation of amorphous Ni-Zr alloy powder by mechanical alloying of intermetallic powder mixtures and mixtures of nickel or zirconium with intermetallics," *Journal of Materials Science*, vol. 23, pp. 2837-2845, 1988.

[10] A. Calka and A. P. Radinski, "Universal high performance ball-milling device and its application for mechanical alloying," *Materials Science and Engineering A*, vol. A134, pp. 1350-1353, 1991.

[11] K. Yamada and C. C. Koch, "The influence of mill energy and temperature on the structure of the TiNi intermetallic after mechanical attrition," *Journal of Materials Research*, vol. 8 (6), pp. 1317-26, 1993.

[12] J. L. Harringa, B. A. Cook, and B. J. Beaudry, "Effects of vial shape on the rate of mechanical alloying," *Journal of Materials Science*, vol. 27, pp. 801-804, 1992.

[13] A. Calka, J. I. Nikolov, and B. W. Ninham, *Mechanical Alloying for Structural Applications*. ASM International, pp. 189-195, 1993.

[14] L. Takacs and M. Pardavi-Horvath, "Nanocomposite formation in the Fe3O4-Zn system by reaction milling," *Journal of Applied Physics*, vol. 75, pp. 5864-5866, 1994.

[15] M. S. El-Eskandarany, K. Aoki, H. Itoah, and K. Suzuki, "Effect of ball-to-powder weight ratio on the amorphization reaction of $Al_{50}Ta_{50}$ by ball milling," *Journal of the Less common Metals*, vol. 169 (2), pp. 235-244, 1991.

[16] W. Lee and S. I. Kwun, "The Effects of process control agents on mechanical alloying mechanisms in the Ti-Al system," *Journal of Alloys and Compounds*, vol. 240, pp. 193-199, 1996.

[17] J. Xu, J. H. He, and E. Ma, "Effect of milling temperature on mechanical alloying in the immiscible Cu-Ta system," *Metallurgical and Materials Transactions A: Physical Metallurgy and Materials Science*, vol. 28 A (7), pp. 1569-1580, 1997.

[18] S. S. Ryu, S. W. Kim, Y. D. Kim, and I. H. Moon, "Amorphization of immiscible W-Cu-Pb system by mechanical alloying at low temperatures," *Journal of Metastable and Nanocrystalline Materials*, vol. 15-16, pp. 313-318, 2003.

[19] C. Suryanarayana, Ed., *Non-equilibrium Processing of Materials*. Pergamon Press, 1999.

[20] Z. Fu and W. L. Johnson, "Nanophase Zr-Al solid solutions by mechanical alloying at elevated temperatures," *Nanostructured Materials*, vol. 3, pp. 175-180, 1993.

[21] E. Gaffet, M. Harmelin, and F. Faudot, "Far-from-equilibrium phase transition induced by mechanical alloying in the Cu-Fe system," *Journal of Alloys and Compounds*, vol. 194, pp. 23-30, 1993.

[22] C. Suryanarayana and H. Jones, "Formation and characteristics of quasicrystalline phases: A review," *International Journal of Rapid Solidification*, vol. 3, pp. 253-293, 1988.

[23] E. Ivanov, I. G. Konstanchuk, B. D. Bokhonov, and V. V. Boldyrev, "Mechanochemical synthesis of icosahedral phases in Mg-Zn-Al and Mg-Cu-Al alloys," *Reactivity of Solids*, vol. 7, pp. 167-172, 1989.

[24] J. Eckert, L. Schultz, and K. Urban, "Formation of quasicrystals by mechanical alloying," *Applied Physics Letters*, vol. 55, pp. 117-119, 1989.

[25] S. Martelli, G. Mazzone, and M. Vittori-Antisari, "The Effect of plastic deformation near room temperature on the solid state reactions between Ni and Sn," *Journal of Materials Research*, vol. 6 (3), pp. 499-504, 1991.

[26] X. Wen-Jie, T. Xin-Feng, and Z. Qing-Jie, "Fast preparation and thermal transport property of TiCoSb based half Heusler compounds," *Chinese Physics*, vol. 16 No 11, pp. 1009-1963, 2007.

[27] J. S. Robinson, P. G. McCormic, and R. Street, "Structure and properties of cu2mnal synthesized by mechanical alloying," *Journal of Physics: Condensed Matter*, vol. 7, pp. 4259-4269, 1995.

[28] M. Atzmon, "In situ thermal observation of explosive compound-formation reaction during mechanical alloying," *Physical Review Letters*, vol. 64 (4), pp. 487-490, 1990.

[29] C. C. Koch, "Rapid solidification of intermetallic compounds," *International Materials Reviews*, vol. 33 (4), pp. 201-219, 1988.

[30] H. Bakker, G. F. Zhou, and H. Yang, "Mechanically driven disorder and phase transformations in alloys," *Progress in Materials Science*, vol. 39 (3), pp. 159-241, 1995.

[31] K. E. Drexler, *Nanosystems: Molecular Machinery, Manufacturing, and Computation*. John Wiley & Sons, Inc, 1992.

[32] E. Hellstern, H. J. Fecht, C. Garland, and W. L. Johnson, "Structural and thermodynamic properties of heavily mechanically deformed Ru and AlRu," *Journal of Applied Physics*, vol. 65 (1), pp. 305-310, 1989.

[33] J. Eckert, J. C. H. Ill, C. E. Krill, and W. L. Johnson, "Structural and thermodynamic properties of nanocrystalline fcc metals prepared by mechanical attrition," *Journal of Materials Research*, vol. 7 (7), pp. 1751-1761, 1992.

[34] T. J. Seebeck, "Magnetische polarisation der metalle and erze durck temperatur-differenz," *Abh. K. Akad. Wiss*., Berlin, p. 265, 1823.

[35] J. C. Peltier, "Nouvelles experiences sur la caloriecete des courans electriques," *Ann. Chem*., vol. LVI, pp. 371-387, 1834.

[36] H. Lenz, *Pogg. Ann*., vol. 44, p. 342, 1838.

[37] D. M. Rowe, Ed., *CRC Handbook of Thermoelectrics*. CRC Press, 1995.

[38] E. Altenkirch, *Physikalische Zeitschrift*, vol. 10, pp. 560-580, 1909.

[39] E. Altenkirch, *Physikalische Zeitschrift*, vol. 12, pp. 920i924, 1911.

[40] R. Yang, A. Narayanaswamy, and G. Chen, "Surface-plasmon coupled nonequilibrium thermoelectric refrigerators and power generators," *Journal of Computational and Theoretical Nanoscience*, vol. 2 (1), pp. 75-87, 2005.

[41] A. F. Ioffe, *Semiconductor Thermoelements and Thermoelectric Cooling*. Infoserach, 1957.

[42] F. Heusler, "Über magnetische manganlegierungen," *Verhandlungen der Deutschen Physikalischen* Gesellschaft, vol. 5, p. 219, 1903.

[43] A. A. Knowlton and O. C. Clifford, "The Heusler alloys," *Transactions of the Faraday Society*, vol. 8, pp. 195-206, 1912.

[44] M. Mikami, A. Matsumoto and K. Kobayashi, "Microstructure and thermoelectric properties of pulse-current sintered Fe2VAl alloy," in *Proceedings ICT'06 - 25th International Conference on Thermoelectrics*, 2006.

[45] W. Jeitschko, "Transition metal stannides with MgAgAs and MnCu(2)Al type structure," *Metallurgical Transactions*, vol. 1, p. 3159, 1970.

[46] F. G. Aliev, N. B. Brandt, V. V. Moshchlkov, V. V. Kozyrkov, R. V. Skolozdra, and A. I. Belogorokhov, "Gap at the fermi level in the intermetallic vacancy system RNiSn(R = Ni, Zr, Hf)," *Physics B – Condensed Matter*, vol. 75, pp. 167-171, 1989.

[47] B. A. Cook, J. L. Harringa, and Z. S. T. and W. A. Jesser, "TiNiSn: A gateway to the (1,1,1) intermetallic compounds," in *15th International Conference on Thermoelectrics*, 1996, pp. 123-127.

[48] B. A. Cook, G. P. Meisner, J. Yang, and C. Uher, "High temperature thermoelectric properties of MNiSn (M=Zr, Hf)," in *18th International Conference on Thermoelectrics*, 1999, pp. 64-67.

[49] C. Uher, J. Yang, and G. P. Meisner, "Thermoelectric properties of bi-doped half-Heusler alloys," in *18th International Conference on Thermoelectrics*, 1999, pp. 56-59.

[50] V. Ponnambalam, A. L. Pope, S. Bhattacharya, S. J. Poon, and T. M. Tritt, "Effect of substitution on the transport properties of the half-Heusler alloy ZrNiSn," in *18th International Conference on Thermoelectrics*, 1999.

[51] V. M. Browning, S. J. Poon, T. M. Tritt, A. L. Pope, S. Bahattacharya, P. Volkov, J. G. Song, V. Ponnambalam, and A. C. Ehrlich, "Thermoelectric properties of the half-Heusler compound (Zr,Hf)(Ni,Pd)Sn," *Materials Research Society Symposium Proceedings*, vol. 545, pp. 403-412, 1999.

[52] H. Hohl, A. P. Ramirez, C. Goldmann, G. Ernst, B. Wolfing, and E. Bucher, "Efficient dopants for ZrNiSn-based thermoelectric materials," *Journal of Physics: Condensed Matter*, vol. 11, pp. 1697-1709, 1999.

[53] Q. Shen, L. Zhang, L. Chen, T. Goto, and T. Hirai, "Thermoelectric properties of ZrNiSn-based half-Heusler compounds by solid state reaction method," *Journal of Materials Science Letters*, vol. 20, pp. 2197-2199, 2001.

[54] B. A. Cook, B. J. Beaudry, J. L. Harringa, and W. J. Barnett, "The preparation of SiGe thermoelectric materials by mechanical alloying," *Proceedings of the Intersociety Energy Conversion Engineering Conference*, vol. 2, pp. 693-700, 1989.

[55] M. Mikami, A. Matsumoto, and K. Kobayashi, "Synthesis and thermoelectric properties of microstructural Heusler Fe2VAl alloy," *Journal of Alloys and Compounds*, vol. 461, pp. 423-426, 2008.

[56] P. Amornpitoksuk and S. Suwanboon, "Correlation of milling time on formation of TiCoSb phase by mechanical alloying," *Journal of Alloys and Compounds*, vol. 462, pp. 267-270, 2008.

[57] S. Bhattacharya, Y. Xia, V. Ponnambalam, S. J. Poon, N. Thadani, and T. M. Tritt, "Reductions in the lattice thermal conductivity of ball-milled and shock compacted TiNiSn(1-x)Sb(x) half-Heusler alloys," in *Thermoelectric Materials 2001-Research and Applications*, G. S. Nolas, D. C. Johnson, and D. G. Mandrus, Eds., vol. 691, 2002, pp. 155-160.

[58] K. Sridhar and K. Chattopadhyay, "Synthesis by mechanical alloying and thermoelectric properties of Cu2Te," *Journal of Alloys and Compounds*, vol. 264, pp. 293-298, 1998.

[59] C. Lee, Y.-H. Park, and H. Hashimoto, "Effect of nanostoichiometry on the thermoelectric properties of a Ag2Se alloy prepared by a mechanical alloying process," *Journal of Applied Physics*, vol. 101, p. 024920, 2007.

[60] W.S. Liu, B.-P. Zhang, J.-F. Li, H.-L. Zhang, and L.-D. Zhao, "Enhanced thermoelectric properties in CoSb(3-x)Te(x) alloys prepared by mechanical alloying and spark plasma sintering," *Journal of Applied Physics*, vol. 102, p. 103717, 2007.

[61] A. F. May, J.-P. Fleurial, and G. J. Snyder, "Thermoelectric performance of lanthanum telluride produced via mechanical alloying," *Physical Review B*, vol. 78, p. 125205, 2008.

[62] M. Zakeri, M. Allahkarami, G. Kavei, A. Khanmohammadian, and M. R. Rahimipour, "Low temperature synthesis of nanocrystalline Sb2Te3 by mechanical alloying," *Journal of Material Sciences*, vol. 43, pp. 1638-1643, 2008.

[63] L.D. Zhao, B.-P. Zhang, W.-S. Liu, H.-L. Zhang, and J.-F. Li, "Enhanced thermoelectric properties of bismuth sulfide polycrystals prepared by mechanical alloying and spark plasma sintering," *Journal of Solid State Chemistry*, vol. 181, pp. 3278-3282, 2008.

[64] C. Uher, S. Hu, J. Yang, G. P. Meisner, and D. T. Morelli, "Transport properties of ZrNiSn-based intermetallics," in *16 International conference on Thermoelectrics*, 1997.

[65] S. R. Culp, S. J. Poon, N. Hickman, T. M. Tritt and J. Blumm. “Effect of substitutions on the thermoelectric figure of merit of half-Heusler phases at 800 C,” *Applied Physics Letters*, vol. 88, pp 042106.

[66] Q. Shen, L. M. Zhang, L. D. Chen, T. Goto, and T. Hirai, “Synthesis and sintering of ZrNiSn thermoelectric compounds,” in *21st International Conference on Thermoelectrics*, 2002, pp. 166-169.

[67] Q. Shen, L. Chen, T. Goto, T. Hirai, J. Yang, G. P. Meisner, and C. Uher, “Effects of partial substitution of Ni by Pd on the thermoelectric properties of ZrNiSn-based half-Heusler compounds,” *Applied Physics Letters*, vol. 79 (25), pp. 4165-4167, 2001.

[68] X. Y. Huang, Z. Xu, and L. D. Chen, “The thermoelectric performance of ZrNiSn/ZrO2 composites,” *Solid State Communications*, vol. 130, pp. 181-185, 2004.

[69] C. Yu, T.-J. Zhu, R.-Z. Shi, Y. Zhang, X.-B. Zhao, and J. He, “High-performance half-Heusler thermoelectric materials Hf(1-x)Zr(x)NiSn(1-y)Sb(y) prepared by levitation melting and spark plasma sintering,” *Acta Materialia*, vol. 57, pp. 2757-2764, 2009.

[70] S. Bhattacharya, V. Ponnambalam, A. L. Pope, P. N. Alboni, Y. Xia, T. M. Tritt, and S. J. Poon, “Thermoelectric properties of Sb-doping in the TiNiSn(1-x)Sb(x) half-Heusler system,” in *18th International Conference on Thermoelectrics*, 1999.

[71] S. Bhattacharya, A. L. Pope, R. T. L. IV, T. M. Tritt, V. Ponnambalam, Y. Xia, and S. J. Poon, “Effect of Sb doping on the thermoelectric properties of Ti-based half-Heusler compounds, TiNiSn(1-x)Sb(x),” *Applied Physics Letters*, vol. 77 (16), pp. 2476-2478, 2000.

[72] S. Bhattacharya, M. J. Skove, M. Russell, T. M. Tritt, Y. Xia, V. Ponnambalam, S. J. Poon, and N. Thadhani, “Effect of boundary scattering on the thermal conductivity of TiNiSn-based half-Heusler alloys,” *Physical Review B*, vol. 77, p. 184203, 2008.

[73] N. J. Takas, H. Zhao, P. F. P. Poudeu, “Thermoelectric Performance of Bulk Zr0.5Hf0.5Co1-xIrxSb0.99Sn0.01 Half-Heusler Alloys,” *2009 MRS Fall Meeting*, 2009

[74] R. Jenkins and R. L. Snyder, *Introduction to X-ray Powder Diffractometry*. John Wiley & Sons, Inc, 1996.

[75] H. P. Klug and L. E. Alexander, *X-Ray Diffraction Procedures For Polycrystalline and Amorphous Materials*, 2nd ed. John Wiley & Sons, 1974.

[76] W. Bragg, “The diffraction of short electromagnetic waves by a crystal,” *Proceedings of the Cambridge Philosophical Society*, vol. 17, pp. 43-57, 1913.

[77] P. P. Ewald, “Das 'reziproke gitter' in der strukturtheorie,” *Z. Kristallogr.*, vol. 56, p. 129, 1921.

[78] P. Scherrer, *Gottinger Nachrichten*, vol. 2, p. 98, 1918.

[79] A. L. Patterson, "The Scherrer formula for x-ray particle size determination," *Physical Review*, vol. 56, pp. 978-982, 1939.

[80] A. R. Stokes and A. J. C. Wilson, "The diffraction of x-rays by distorted crystal aggregates - I," *Physical Society*, vol. 3, pp. 174-181, 1944.

[81] G. K. Williamson and W. H. Hall, "X-ray line broadening from filed aluminum and wolfram," *Acta Metallurgica*, vol. 1, pp. 22-31, 1953.

[82] *Standard Test Method for Young's Modulus, Tangent Modulus , and Chord Modulus*, ASTM Std. E111- 97.

[83] Y. Gelbstein, G. Gotesman, Y. Lishzinker, Z. Dashevsky, and M. P. Dariel, "Mechanical properties of PbTe-based thermoelectric semiconductors," *Scripta Materialia*, vol. 58, pp. 251-254, 2008.

[84] S. Urata, R. Funahashi, T. Mihara, A. Kosuga, and N. Miyasou, "Mechanical properties of oxide materials," in *Proceedings ICT'07 - 26th International Conference on Thermoelectrics*, 2007.

[85] D. Vasilevskiy, F. Roy, E. Renaud, R. Masut, and S. Turenne, "Mechanical properties of the interface between nickel contact and extruded (bi1-xsbx)2(te1-ysey)3 thermoelectric materials," in Proceedings *ICT'06 - 25th International Conference on Thermoelectrics*, 2006.

[86] X. Wu, G. Xu, Y. Xu, C. Zhang, and C. Ge, "Mechanical and thermoelectric performance of p-type Bi-Sb-Te prepared by hot pressing," in *Proceedings ICT'06 - 25th International Conference on Thermoelectrics*, 2006.

[87] R. N. Grass, T. F. Albrecht, F. Krumeich, and W. J. Stark, "Large-scale preparation of ceria/bismuth metal-matrix nano-composites with a hardness comparable to steel," *Journal of Materials Chemistry*, vol. 17, pp. 1485-1490, 2007.

[88] D. B. Marshall, T. Noma, and A. G. Evans, "A simple method for determining elastic-modulus-to hardness ratios using Knoop indentation measurements," *American Ceramic Society Bulletin*, vol. 65, pp. C175-C176, 1982.

[89] F. Ren, E. D. Case, E. J. Timm, and H. J. Schock, "Young's modulus as a function of composition of an n-type lead-antimony-silver-telluride (last) thermoelectric material," *Philosophical Magazine*, vol. 87 (31-33), pp. 4907-4934, 2007.

[90] W. C. Oliver and G. M. Pharr, "Measurement of hardness and elastic modulus by instrumented indentation: Advances in understanding and refinements to methodology," *Journal of Materials Research,* vol. 19 (1), pp. 3-20, 1994.

[91] F. Ren, E. D. Case, E. J. Timm and H. J. Schock, "Hardness as a function of composition for n-type last thermoelectric material," *Journal of Alloys and Compounds*, vol. 455, pp. 340-345, 2008.

[92] A. G. Evans and E. A. Charles, "Fracture toughness determinations by indentation," *Journal of the American Ceramic Society*, vol. 59 (7-8), pp. 371 - 372, 1976.

[93] B. R. Lawn and E. R. Fuller, "Equilibrium penny-like cracks in indentation fracture," *Journal of Materials Science*, vol. 10, pp. 2016-2024, 1975.

[94] B. R. Lawn and M. V. Swain, "Microfracture beneath point indentations in brittle solids," *Journal of Materials Science*, vol. 10, pp. 113-122, 1975.

[95] R. H. Marion, "Use of indentation fracture to determine fracture toughness," in *Fracture Mechanics Applied to Brittle Materials*, ASTM STP 678, S. W. Freiman, Ed. American Society for Testing and Materials, 1979, pp. 103-111.

[96] J. B. Wachtman, W. R. Cannon, and M. J. Matthewson, *Mechanical Properties of Ceramics.* John Wiley & Sons, 2009.

[97] K. Ueno, A. Yamamoto, T. Noguchi, T. Inoue, S. Sodeoka, and H. Obara, "Optimization of hot-press conditions of Zn4Sb3 for high thermoelectric performance. ii. mechanical properties," *Journal of Alloys and Compounds*, vol. 388, pp. 118-121, 2005.

[98] L.-D. Zhao, B.-P. Zhang, J.-F. Li, M. Zhou, W.-S. Liu, and J. Liu, "Thermoelectric and mechanical properties of nano-SiC-dispersed Bi2Te3 fabricated by mechanical alloying and spark plasma sintering," *Journal of Alloys and Compounds*, vol. 455, pp. 259-264, 2008.

[99] A. Migliori, J. Sarrao, W. M. Visscher, T. M. Bell, M. Lei, Z. Fisk, R. G. Leisure, "Resonant ultrasound spectroscopic techniques for measurement of the elastic moduli of solids," *Phsyica B.* vol. 183, pp. 1-24, 1993.

[100] F. Ren, B. D. Hall, J. E. Ni, E. D. Case, J. Sootsman, M. G. Kanatzidis, E. L. Curzio, R. M. Trejo, and E. J. Timm, "Mechanical characterization or PbTe-based thermoelectric materials," in *Material Research Society Symposia Proceedings*, vol. 1044, 2008.

[101] ICDD, "JCPDS reference pattern 23-1281."

[102] *X'Pert PRO User's Guide*, Philips Analytical B. V., Lelyweg 1 P.O.box 13 7600 AA Almelo The Netherlands, 2002.

[103] *XP CSM standard hardness, modulus, and tip cal, TestWorks 4*, Agilent Technologies, Oak Ridge, TN. Testworks 4 ed., Agilent Technologies, Oak Ridge, TN.

[104] C. Suryanarayna, *Mechanical Alloying and Milling*. Marcel Dekkar, 2004.

[105] R. Schulz, M.L.Trudeau, A. Van Neste, "The contribution of strain and plastic deformations to the amorphization reaction of Ni---Zr alloys by mechanical alloying," *Materials Science and Engineering: A*, vol. 134, pp 1354 – 1360, 1991.

[106] D. H. Wen, Y. H. Wan, and T. Hong, "Surface integrity induced by abrasive machining sapphire wafer," *Advanced Materials Research*, vol. 53-54, pp. 311-316, 2008.

[107] K. Brazier, www.widipedia.org/wiki/File:Themoelectric_Generator_Diagram.svg, 2008

[108] M. G. Kanatzidis, "Nanostructured Thermoelectrics: The New Paradigm" *Chemistry of Materials: Review*, vol. 22, pp 648-659, 2010.

[109] Newage Testing Instruments, www.hardnesstesters.com

[110] L.D. Zhao, B.P Zhang, W.S Liu, J.F. Li, "Effect of mixed grain sizes on thermoelectric performance of Bi(2)Te(3) compounds," *Journal of Applied Physics Letters*, vol. 105, pp. 203704, 2009.

[111] A. Calka, D. Wexler, "A study of the evolution of particle size and geometry during ball milling," *Materials Science Forum*, vol. 360-362, pp 301-310, 2001.

[112] C. R. Nave, "http://hyperphysics.phy-astr.gsu.edu," Georgia State University, 2006

[113] *User Guide NanoIndenter G200,* MTS Systems Corporation.

Jeffrey D. Germond was born in Stoughton, Wisconsin and received his B. S. in Physics from the University of Michigan.